WOOD AND FIBER SCIENCE

The Sustainable Natural Materials Journal

Volume 54, Number 4_2022 *(ISSN 0735-6161)*

Open Access

JOURNAL OF THE

SWST – International Society of Wood Science and Technology

SOCIETY OF WOOD SCIENCE AND TECHNOLOGY

2022–2023 Officers of the Society

President: Henry Quesada, Purdue University, Indiana, USA
Immediate Past President: Rupert Wimmer, BOKU Vienna, Austria
President-Elect: Jeffrey Morrell, University of the Sunshine Coast, Australia
Vice President: Ilona Peszlen, North Carolina State University, Raleigh, NC
Executive Director: Victoira Herian, Society of Wood Science and Technology, P.O. Box 6155, Monona, WI 53716-1655, vicki@swst.org
Directors:
Omar Espinoza, University of Minnesota, St. Paul, MN 55108
Judith Gisip, Universiti Teknologi MARA, Malaysia
Hongmei Gu, USDA Forest Products Laboratory, Madison, WI 53726
Francesco Negro, DISAFA – University of Torino, Italy
Editor, Wood and Fiber Science: Susan LeVan-Green, sue.levangreen@gmail.com
Associate Editor, Wood and Fiber Science: Arijit Sinha, Oregon State University, Corvallis, OR 97331, arijit.sinha@oregonstate.edu
Digital Communication Coordinator: Pipiet Larasatie, Oregon State University, Corvallis, OR 97331, pipiet.larasati@gmail.com
Editor, BioProducts Business Editor: Eric Hansen, Oregon State University, Corvallis, OR 97331, eric.hansen@oregonstate.edu

WOOD AND FIBER SCIENCE

Wood and Fiber Science is published quarterly in January, April, July, and October by the Society of Wood Science and Technology, P.O. Box 6155, Monona, WI 53716-6155

Editor
Susan LeVan-Green
sue.levangreen@gmail.com
Associate Editors
Arijit Sinha
Oregon State University
arijit.sinha@oregonstate.edu

Editorial Board

Stergio Adamopoulos, Sweden
Babatunde Ajayi, Nigeria
Susan Anagnost, USA
H. Michael Barnes, USA
Claudio Del Menezzi, Brazil
Levente Denes, Hungry
Yusuf Erdil, Turkey
Massimo Fragiacomo, Italy
Fred Franço, USA
Steven Keller, USA
Shujun Li, China
Lucian Lucia, USA
Sameer Mehra, Ireland
John Nairn, USA
Francesco Negro, Italy
Jerrold Winandy, USA
Qinglin Wu, USA

There are three classes of membership (electronic only) in the Society: Members – dues $150; Retired Members – dues $75; Student Members – dues $50. We also have membership category for individuals from Emerging Countries where individual members pay $30, individual students pay $10; Emerging Group of 10 pay $290, and Student Groups of 10 pay $90. Institutions and individuals who are not members pay $300 per volume (electronic only). Applications for membership and information about the Society may be obtained from the Executive Director, Society of Wood Science and Technology, P.O. Box 6155, Monona, WI 53716-6155 or found at the website http://wwww.swst.org.

Site licenses are also available with a charge of:
- $300/yr for single online membership, access by password and email
- $500/yr for institutional subscribers with 2–10 IP addresses
- $750/yr for institutional subscribers with 11–50 IP addresses
- $1000/yr for institutional subscribers with 51–100 IP addresses
- $1500/yr for institution subscribers with 101–200 IP addresses
- $2000/yr for institutions subscribers with over 200 IP addresses.

New subscriptions begin with the first issue of a new volume. All subscriptions are to be ordered through the Executive Director, Society of Wood Science and Technology.

The Executive Director, at the Business Office shown below, should be notified 30 days in advance of a change of email address.

Business Office: Society of Wood Science and Technology, P.O. Box 6155, Monona, WI 53716-6155.
Editorial Office: Susan LeVan-Green, sue.levangreen@gmail.com

WOOD AND FIBER SCIENCE

JOURNAL OF THE SOCIETY OF WOOD SCIENCE AND TECHNOLOGY

VOLUME 54 OCTOBER 2022 NUMBER 4

EDITOR'S NOTE

As 2022 ends, so does my tenure as the Editor of ***Wood and Fiber Science***. I have thoroughly enjoyed my time as the Editor and have continued learning about the wonderful research ongoing in the field of wood science. I wish you all well in your future research efforts.

At this time, I would like to thank all the reviewers who helped make the 2022 Issue (Volume 54) a success, their names follow:

THANKS TO OUR REVIEWERS

Jerry Oppong Adutwum
Michael David Burnard
Zeki Candan
Daniel Ciolkosz
Joseph Dahlen
Benjamin Dawson-Ando
Levente Denes
Iris Beatriz Vega Erramuspe
Akinsanmi Fowowe
Frederico Jose Nistal Franca
Thomas Gorman
Massimo Gragiacomo
Khaled T.S. Hassan
Eva Haviarova
Steven Keller
Pipiet Larasatie
Shujun Li
Vahid Mahdavifar
Jeffrey Morrell
Roger Moya
Francesco Negro
Mehran Roohnia
Christopher Adam Senalik
Robert Smith
Forence Pascua Soriano
C. Elizabeth Stokes
Ales Straze
Luvuyo Tyhoda
Patricia Vega
Xiping Wang,
Daniel Way
Jerrold Winandy
Qinglin Wu

Again, thank you to all these reviewers who provide diligent and helpful comments to the authors. The reviewers are the backbone of this journal.

The new Editor is Jeffrey Morrell, who is an Emeritus Professor of Oregon State University and is serving as the Director of the National Centre for Timber Durability & Design Life at the University of the Sunshine Coast in Queensland, Australia. Jeff has many years publishing scientific articles and is well-known in the academic circle. He will do an outstanding job.

My parting comment is to encourage scientists to publish in *Wood and Fiber Science*. We have made strides ensuring this journal is a high quality scientific, professional journal for those of you in the wood science field.

https://doi.org/10.22382/wfs-2022-21
© 2022 by the Society of Wood Science and Technology

PERFORMANCE OF TIMBER BOARD MODELS FOR PREDICTION OF LOCAL BENDING STIFFNESS AND STRENGTH—WITH APPLICATION ON DOUGLAS FIR SAWN TIMBER

*A. Olsson**

Professor
Department of Building Technology
Linnaeus University
Växjö, Sweden
E-mail: anders.olsson@lnu.se

G. Pot

Associate Professor
Arts et Métiers Sciences et Technologies
LABOMAP Université Bourgogne Franche-Comté
HESAM Université, F-71250
Cluny, France
E-mail: guillaume.pot@ensam.eu

J. Viguier

Associate Professor
Arts et Métiers Sciences et Technologies
LABOMAP, Université Bourgogne Franche-Comté
HESAM Université, F-71250
Cluny, France
E-mail: joffrey.viguier@ensam.eu

M. Hu

Assistant Professor
Department of Building Technology
Linnaeus University
Växjö, Sweden
E-mail: min.hu@lnu.se

J. Oscarsson

Associate Professor
Department of Building Technology
Linnaeus University
Växjö, Sweden
E-mail: jan.oscarsson@lnu.se

(Received April 2022)

Abstract. Efficient utilization of structural timber requires accurate methods for machine strength grading. One of the most accurate methods presented this far is based on data of local fiber orientation on board surfaces, obtained from laser scanning. In this paper, two potential improvements of this method are examined. The first one consists of replacing a model based on simple integration over cross sections of boards for calculation of local bending stiffness by a 3D solid finite element (FE) model from which local bending stiffness is derived. The second improvement concerns replacement of a simple model for the fiber orientation in the interior of board by a more advanced one taking location of pith and growth direction of knots

* Corresponding author

into account. Application of the alternative models on a sample of more than 200 Douglas fir boards, size 40 mm × 100 mm × 3000 mm, cut from large logs, show that each of the evaluated model improvements contributes to improved grading accuracy. When local bending stiffness is calculated utilizing the herein suggested FE model in combination with the improved model of fiber orientation in the interior of boards, a coefficient of determination to bending strength as high as 0.76 is obtained. For comparison, a coefficient of determination of 0.71 is obtain using the simpler original models.

Keywords: Dynamic excitation, lumber, modulus of elasticity, modulus of rupture, stress grading, tracheid effect.

INTRODUCTION

Strength and stiffness of timber vary substantially between pieces and therefore effective utilization of structural timber requires machine strength grading, using indicating properties (IPs), and machines by which strength could be predicted with a certain level of accuracy. In many of the methods and machines used on the market today, especially in Europe, the longitudinal dynamic modulus of elasticity (MoE) is utilized as an IP to edgewise bending or tensile strength (Oscarsson 2014). The vibration signal from dynamic excitation, the weight or the density, and the dimensions of the board can be measured fast and accurately with machines that are comparatively inexpensive, and the dynamic MoE, representing an average MoE of the board, is calculated using a simple equation. However, the relationship between longitudinal dynamic MoE and strength is rather weak. For Norway spruce (*Picea abies*) the coefficient of determination, R^2, between longitudinal dynamic MoE and edgewise bending strength is often about 0.5 or slightly higher when linear regression is applied (Hanhijärvi and Ranta-Maunus 2008; Olsson and Oscarsson 2017) and differs between different samples and investigations. For Douglas fir, the coefficient of determination between dynamic MoE and bending strength is often lower than for spruce. Olsson et al (2018a) reported an R^2 of 0.47 for a sample of more than 800 structural sized Douglas fir timber boards of mixed dimensions.

There are grading machines on the market in which high-resolution X-ray scanning is combined with dynamic MoE. This combination of techniques represents the most accurate strength grading method of those common on the market today (Briggert et al 2020). The information added by X-ray scanning concerns the variation of density within a board which means that knot measures can be derived and used in definitions of IPs. In an extensive study performed by Hanhijärvi and Ranta-Maunus (2008), comprising more than 1000 boards of Norway spruce and 1000 boards of Scots pine (*Pinus sylvestris*), assessments of various strength grading machines and of the relationship between IPs and strength in both tension and bending were performed. The method/IP that showed the best performance, with respect to coefficient of determination between IP and bending or tensile strength, was based on a combination of data from dynamic excitation and X-ray scanning. For Norway spruce timber, loaded to failure in bending, this method/IP gave an R^2 to bending strength of 0.64. When dynamic MoE (also assessed by equipment from the same company) was calculated on the basis of resonance frequency and board density, and on resonance frequency alone, R^2 of 0.57 and 0.48, respectively, were achieved for the same timber. For the sample of Scots pine, the improvement in grading accuracy when using the method/IP based on the combination of X-ray scanning and dynamic MoE, rather than on dynamic MoE alone, was larger than what it was for the sample of Norway spruce. Other studies that give examples of the performance of the same or similar equipment are Bacher (2008) and Nocetti et al (2010).

Olsson et al (2013) suggested a strength grading method based on dot laser scanning and utilization of the tracheid effect (Matthews and Beech 1976; Soest et al 1993; Briggert et al 2018), which gives high-resolution information of the fiber orientation on board surfaces, and knowledge of dynamic MoE. Based on knowledge of local fiber orientation, wood material stiffness properties in

orthogonal directions, and calculation of board stiffness on the cross-sectional level using a rather simple integration model, an IP defined as the lowest local edgewise bending MoE found along a board was established. Comprehensive investigations on a large sample of Norway spruce boards of mixed dimensions (Olsson and Oscarsson 2017) and on samples of Norway spruce, Douglas fir, and European oak, respectively (Olsson et al 2018a), showed that application of this method gives accurate predictions of bending strength and high yields in high strength classes. For example, coefficients of determination to bending strength of about 0.68-0.70 was achieved for Norway spruce. For Douglas fir, the method has up until now only been evaluated for one sample, consisting of about 800 boards of three different dimensions (Olsson et al 2018a), which gave a coefficient of determination to bending strength of 0.62 (compared with 0.47 using dynamic MoE as IP). Furthermore, this method has also been used for prediction of tensile strength of glulam lamellas. In a study by Briggert et al (2020) on a sample of more than 900 Norway spruce boards of mixed dimensions, a coefficient of determination to tensile strength of 0.66 (using linear regression) and 0.70 (using nonlinear regression) was obtained. For the same sample, a coefficient of determination of 0.46 (linear regression) was obtained using dynamic MoE as IP to tensile strength. Briggert et al (2020) also showed that the method based on fiber orientation detected on surfaces gives almost as accurate prediction of strength when applied on Norway spruce boards with sawn surfaces as when applied on boards with planed surfaces. So far, no other method that gives more accurate predictions of strength when assessed on large samples of sawn timber, ie samples large enough to give basis for settings for a machine controlled strength grading method (EN 14081-2 2018), seems to exist. However, there is potential for improvements of the method. This was shown by Hu et al (2018) who suggested 1) a new way to estimate the fiber direction in the interior of a board by utilizing knowledge of location of pith in relation to the board cross section and 2) use of a 3D finite element (FE) model, rather than simple integration over the cross section, to calculate local bending stiffness. In Hu et al (2018), local bending stiffness was calculated on the basis of fiber direction data from laser scanning of two Norway spruce boards, using the original as well as improved versions of the method/model, and the results were compared with local bending stiffness calculated on the basis of local strains, obtained from digital image correlation (DIC) of the boards when they were subjected to constant bending moment. Comparisons for the two boards included in that study showed that suggested improvements of the model lead to substantial improvement regarding resemblance between bending stiffness profiles obtained based on the model and of DIC, respectively.

Regarding location of pith, new methods to determine this have been developed in the last few years. Habite et al (2020) presented a method to automatically determine location of pith in relation to board cross sections, based on optical scanning of the four longitudinal surfaces of boards and identification of annular ring pattern on images of the surfaces. Faster and more robust methods, based on optical scanning of longitudinal board surfaces in combination with machine learning, were developed by Habite et al (2021) and in particular Habite et al (2022). Thus, it is possible to determine pith location in production speed at sawmills and to utilize this in models of boards.

The objective of the present study is to investigate if the improvements of the method/model, suggested by Hu et al (2018), give more accurate predictions of strength than what the original versions of the method (Olsson et al 2013; Olsson and Oscarsson 2017; Olsson et al 2018a) does, by applying this method on a database of 241 Douglas fir boards.

Before proceeding with the present study, some other recent research works, also aiming at improved modeling and strength grading on sawn timber by utilizing the possibilities of modern scanning techniques and/or FE analyses should be mentioned, namely the following.

- Viguier et al (2017) suggested a grading method based on a combination of data from

tracheid effect scanning and X-ray scanning. In this method, data of local fiber orientation was utilized in a similar way as by Olsson et al (2013) but using the data from the two wide faces only. Furthermore, local density was used to assess local material properties. An elaborate calculation scheme, including assessment of local stresses corresponding to edgewise bending of the board, was used to predict board strength. The method was successfully applied on large samples of Norway spruce and Douglas fir boards and the grading accuracy obtained was similar to the one obtained by Olsson et al (2013) and Olsson and Oscarsson (2017).

- Lukacevic et al (2015) developed a procedure to reconstruct location of pith and 3D knot geometry on the basis of data from traditional, 2D X-ray scanning. The authors used the determined 3D knot geometry as basis for different IPs to bending strength and very high coefficients of determination to strength were obtained, when combining up to seven different predictor variable in linear regression, but the sample size used was too small to prove that the models were reliable. Later the same research group has presented improved models for 3D reconstruction of knots (Kandler et al 2016) and for fiber orientation in the surroundings of knots (Lukacevic et al 2019) on the basis of data from tracheid effect scanning combined with a mathematical model for fiber orientation in 3D around knots developed by Foley (2003).
- Sarnaghi and van de Kuilen (2019) identified size and location of knots manually/visually and established based on such data 3D models of knots and, utilizing a grain flow analogy, local fiber orientation of 102 boards of Norway spruce and 150 boards of Douglas fir. The fiber orientation models in turn gave basis for FE models by which local stresses corresponding to tensile loading of boards were calculated. By performing nonlinear regression utilizing two different stress concentration factors (which were calculated on the basis of stresses from FE simulation) in combination with knowledge of axial dynamic MoE (in total utilizing five predictor variables in the regression model) coefficients of determination to tensile strength of up to 0.75 and 0.72 were obtained for the samples of Norway spruce and Douglas fir, respectively.
- Jenkel and Kaliske (2018) presented an advanced FE model of timber boards including plasticity and fracture mechanics for prediction of tensile strength. Knot geometry and local fiber orientation were determined in a similar way as by Sarnaghi and van de Kuilen (2019). The material and mechanical model suggested may be the most advance one this far used to predict tensile strength of sawn timber but the assumptions made regarding material properties were, in comparison, simple and based on limited experimental data. Regarding comparison of calculated and experimentally determined tensile strength of boards, results were presented only for selected boards and not for a full sample. Thus, coefficients of determination to strength comparable to those obtained from other investigations/methods were not presented.
- As an example of recent work in this field carried out by a non-European research group, Wright et al (2019) automatically identified knots on surfaces of 171 pieces of loblolly pine lumber and based on this evaluated different knot measures for prediction of bending strength of boards.

In summary, several rather similar attempts to develop accurate methods for machine strength grading by utilizing high-resolution data and/or models of boards, including knot geometry and local fiber orientation, have been made in recent years. Further work in this area should consist of systematic and critical assessment of potential improvements regarding—representation of knot geometry and fiber orientation within boards; mechanical, material, and numerical models employed; definitions of IPs—such that the most critical limitations of the methods presented this far are successively identified and eliminated. As explained above, the aim of the present paper is to contribute in this respect.

MATERIAL AND DATA FROM INTRODUCTORY INVESTIGATIONS

Eight logs of Douglas fir (*Pseudotsuga menziesii* [Mirb.] Franco), cultivated in France, were originally selected to investigate structural properties of sawn Douglas fir timber as functions of the distance to pith, and to investigate the accuracy of different methods for machine strength grading when applied on boards from different parts of logs. Therefore, logs with large diameters of about 50 cm were selected. From each such log a large number of boards were cut, including a significant number from outerwood. Herein outerwood boards are defined as boards that are located, at least partly, outside a radius of 200 mm from the pith. From the eight logs, 241 boards (between 24 and 36 boards from each log) of nominal dimensions 40 mm × 100 mm × 3000 mm and without significant wane were sawn and dried in an industrial sawmill. Before sawing, a pattern was painted on the butt-end of each log such that the position of each board could be related to the log cross section also after sawing. In Fig 1, the butt end of log no. 7, and the pattern painted on it, is shown. Indicated in the figure are also the reconstructed position of each of the boards cut from the log, and two coordinate systems used to define coordinates of the entire log cross section and of a single board cross section, respectively. Such coordinate systems were used to determine the position and orientation of each board in relation to the pith of the log. Thus, the material used for the present investigation comprise 241 Douglas fir boards for which position and orientation in relation to the pith of the log are known. The accuracy/error of location of pith should be within a couple of millimeters up to about one centimeter in the butt-end of the boards and up to a few centimeters in the top end of the boards. Since log top-ends were not painted, the accuracy of location of pith was lower in the top-end than in the butt-end.

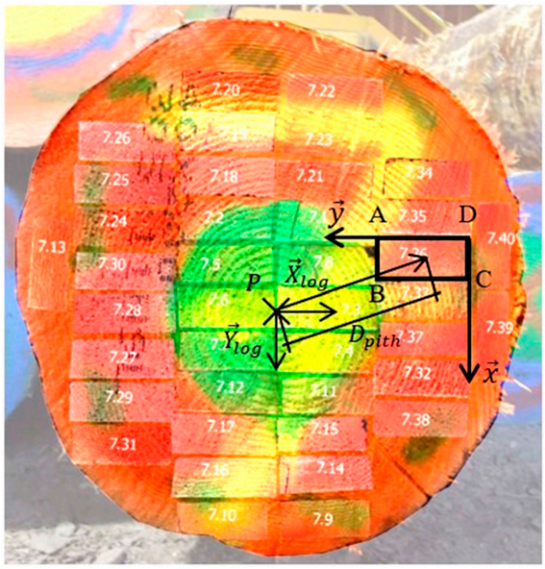

Figure 1. Photomontage of the painted butt-end of one log (no. 7, as an example) with the cross section of the 40 mm × 100 mm sawn boards superposed on it. The 15 annual rings closest to the pith are painted in a different color to enable localization of juvenile wood of the boards cut from the log. For board no. 7.36, framed in black, a local coordinate system ($D, \vec{x}, \vec{y}, \vec{z}$) is indicated. D_{pith} mark the distance between pith and the center of the board cross section. Points A, B, C, and D represent the positions of the four corners of the cross section.

METHODS

Collection of Data and Definitions of Properties

Below it is described how the data from the introductory investigation, in combination with additional measurements, give basis for and are utilized in models and definitions of IPs, and to determine properties like local static MoE and bending strength.

Scanning to obtain fiber orientation, color images, and local density. A CombiScan+ industrial scanner from the company LuxScan Technologies (Weinig group) was used to measure board dimensions, to take red-green-blue (RGB) images of surfaces, to determine local fiber orientation on surfaces and to determine local density of the boards, when the boards are fed longitudinally through the scanner. Local fiber orientation on surfaces was obtained by means of dot lasers and utilization of the tracheid effect, giving a resolution of determined in-plane fiber direction in longitudinal and transversal direction of the

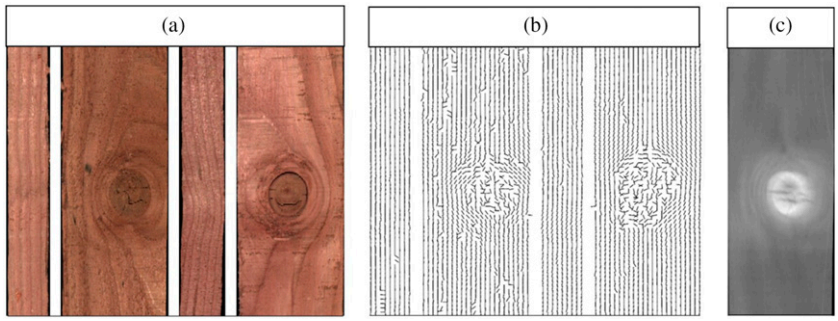

Figure 2. Data obtained using the scanner, displayed for a 250 mm long section of a board; (a) RGB images of four sides of the board, (b) determined in-plane fiber directions on four sides (resolution in longitudinal direction reduced to 4 mm in the images), and (c) determined local density, averaged over the thickness direction, where bright areas represent high density and dark areas represent low density.

board of about 1 mm and 4 mm, respectively, on all four sides of the board. Local density, determined as an average value over the thickness direction of a board, was obtained by means of X-ray giving a resolution in longitudinal and transversal board direction of about 1 mm and 0.3 mm, respectively. However, data of density obtained from X-ray scanning was not utilized in the present investigation. Instead, the density was determined manually, see "Determination of density, moisture content and resonance frequency" section. In Fig 2, examples of data obtained using the scanner is displayed showing, for a 250 mm long section of a board, 1) RGB images of four sides, 2) determined in-plane fiber directions on four sides (resolution in longitudinal direction reduced to 4 mm in the images), and 3) determined local density where bright areas represent high density. Fibers within round knots are almost parallel with the direction of the branch/knot itself, ie the fiber direction is close to perpendicular to the wide faces of the board surfaces displayed. Laser dots illuminating surfaces of round knots become almost circular in shape and the determined in-plane fiber directions become, within the knot areas, more or less randomly oriented. In the surroundings of the knots, in-plane fiber directions resemble flow lines around the knots. Some of the detected local fiber directions, also in clear wood parts of the surfaces, diverge, seemingly randomly, from the longitudinal direction of the board (Fig 2[b]). This is due to the roughness of the sawn wood surfaces, as discussed by Daval et al (2015) and Briggert et al (2020).

Determination of density, MC, and resonance frequency. For each board, the board mass (m), the board length (L), depth (h), and thickness (t) and the board MC (u_s) were determined manually. A scale was used for weighing, and a Gann HT 95 pin-type moisture meter was used to determine the MC. To determine the lowest longitudinal resonance frequency of the board, (f_1), an E-scan machine from LuxScan Technologies was employed.

On the basis of these data the *average board density*, adjusted to 12% MC (MC), was calculated as

$$\rho_{\text{corr}} = \frac{m}{L \cdot h \cdot t}\left(1 - \frac{u_s - 12}{200}\right). \quad (1)$$

Furthermore, the *dynamic axial MoE*, adjusted with respect to MC, was calculated as

$$E_{\text{a,corr}} = 4\frac{m}{L \cdot h \cdot t} f_1^2 L^2 \left(1 + \frac{u_s - 12}{100}\right). \quad (2)$$

The adjustments with respect to MC were done in accordance with the European standard (EN 384 2016).

Destructive Tests and Determination of Local Bending MoE and Bending Stiffness

In Fig 3, the test arrangement for a four-point bending test according to the European standard

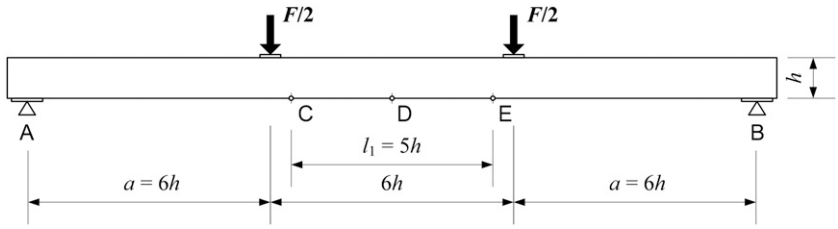

Figure 3. Test setup for determination of local MoE and bending strength in edgewise bending.

(EN 408 2010) is displayed. Based on such a test the local static MoE in bending, adjusted to 12% MC, was determined as

$$E_{m,l} = \frac{a l_1^2 (F_2 - F_1)}{16 I (w_2 - w_1)} \quad (3)$$

where a is the distance between one of the point loads and the closest support, F is the total loading (two load levels, F_1 and F_2, respectively), $l_1 = 5h$ is the span for determination of local MoE, I the second moment of inertia ($th^3/12$) and w the center deflection of the span l_1 (D in relation to C and E, see Fig 3).

When $E_{m,l}$ has been determined in accordance with Eq 3 a correction with respect to MC was performed as

$$E_{m,l,corr} = E_{m,l}\left(1 + \frac{u_s - 12}{100}\right). \quad (4)$$

The bending strength f_m was calculated in accordance with EN 408 as

$$f_m = \frac{3 F_{max}\, a}{b h^2} \quad (5)$$

where F_{max} is the maximum value of the total load applied by the two point loads. This bending strength is then corrected for boards with a depth less than 150 mm, ie the size effect is taken into account, according to the European standard EN 384, clause 5.4.3 as

$$f_{m,h} = \frac{f_m}{k_h} \quad (6)$$

where

$$k_h = \min \begin{cases} \left(\frac{150}{h}\right)^{0.2} \\ 1.3 \end{cases}. \quad (7)$$

In this research, only pieces that broke within the maximum/constant bending zone, ie within the point loads, was considered. Thus, all the boards that broke *outside* the point loads, which was the case for 20 boards, were disregarded for further evaluation which means that $241 - 20 = 221$ boards are considered in the following evaluation.

Models for Calculation of Local Bending Stiffness

Below a summary of the grading method suggested by Olsson et al (2013) is given, followed by descriptions of the improvements of the method suggested by Hu et al (2018).

Stiffness based on integration over cross section. The machine strength grading method (Olsson et al 2013) which is the basis for the present investigation can, in brief, be divided into three steps below:

1. It is assumed that the in-plane fiber direction, represented by an angle, φ, detected locally on a board surface (see Fig 4[a]) is representative for a small area (a few square millimeters, depending on resolution of data of fiber direction) of the surface. Furthermore, the fiber orientation in the interior of the board is a function of the fiber orientation on the surfaces. The original way to determine the fiber orientation in the interior of the board was that φ is applied to a certain depth into the board, ie φ is assumed to be valid for the sub volume $\Delta x \Delta A$, as illustrated in Fig 4(a) and (b).
2. Values of nine independent material parameters of the wood material (MoEs, shear moduli and Poisson's ratios) are adopted. Values for Douglas fir used in the present study are

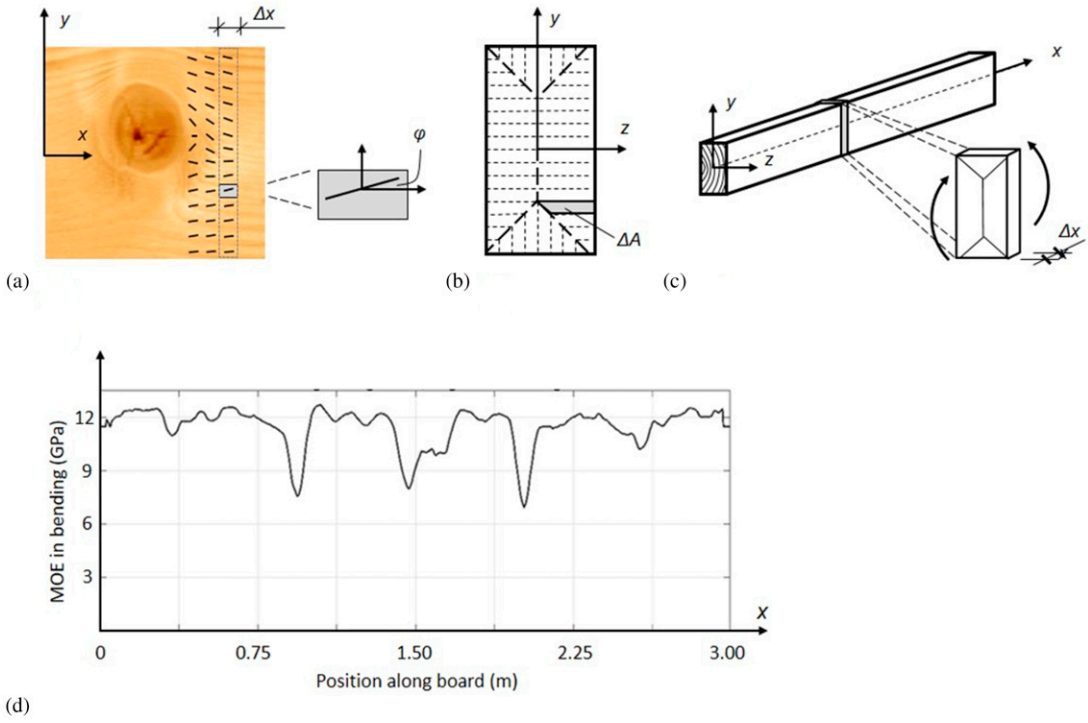

Figure 4. (a) Local in-plane fiber directions identified on a member's surface, (b) cross section divided into subareas implying that the exhibited angle φ and corresponding MoE in the longitudinal direction, $E_x(x, y, z)$, is valid within the volume $\Delta A \Delta x$, (c) segment of length Δx for which the edgewise bending MoE is calculated by stiffness integration over the segment's cross section, and (d) a bending MoE profile, each value along the graph representing the average edgewise bending MoE of the surrounding 90 mm.

identical to those used in Olsson et al (2018a). On the basis of these, and the local fiber direction, the corresponding local MoE, $E_x(x, y, z)$, valid in longitudinal direction x, is calculated by transformation for every position within the volume of the board.

3. The cross-sectional edgewise bending stiffness, for positions x (in steps of Δx) along the board, is calculated by numerical integration over the cross section (see Fig 4[c]) as

$$EI_z(x) = \sum_A E_x (y - \bar{y})^2 \Delta A \qquad (8)$$

where

$$\bar{y} = \frac{\sum_A E_x y \Delta A}{\sum_A E_x \Delta A} \qquad (9)$$

and y is the coordinate in depth direction of the center point of each small subarea ΔA of the cross-sectional area A. Eqs 8 and 9 enable calculation of an edgewise bending MoE, as function of the position along the board, as

$$E_b(x) = \frac{12 EI_z(x)}{th^3} \qquad (10)$$

where t and h are the thickness and depth, respectively, of the board cross sections.

In Fig 4(d), a calculated MoE profile, established by calculating a moving average of $E_b(x)$ over a length of 90 mm is displayed. IPs to bending strength, established on the basis of the lowest value of such MoE-profiles in combination with axial dynamic MoE were evaluated in eg Olsson et al (2013), Olsson and Oscarsson (2017), and Olsson et al (2018a). In the following the method to calculate

bending MoE as described above is referred to as the integration over cross section (IOCS) method.

Finally, two deficiencies of the described method should be pointed out. First, calculation of bending stiffness by integration of stiffness over single cross sections (of very short length, Δx) at a time, before calculating a mean stiffness over a longer distance (eg 90 mm) means that the local bending stiffness is overestimated. In reality, a short segment along the board containing for example two knots at different position in x- and y-direction may have considerably more compliance to bending than what is captured using the IOCS model. Second, the assumptions that fibers are located in the plane of each scanned surface and that the determined fiber angle at the surface is valid to a certain depth into the board, without consideration of the direction of knots within the board, do not reflect the real fiber direction within the board.

Stiffness based on FE method and simulation of bending. As an alternative to the IOCS method, Hu et al (2018) used a 3D FE model and simulation of pure bending to calculate local bending MoE. The FE model consisted of 8-node linear brick, full integration elements. The element size used was 5 mm × 5 mm × 5 mm and a convergence study indicated that this element mesh was sufficient for the present purpose. The basis for material directions locally in the board volume and the material parameters applied were the same as those defined for the IOCS method. Thus, steps (a and b) as described in the "Stiffness based on integration over cross section" section were performed before FE modeling and simulation of constant bending of the part of the board of length $l_1 = 5h$ between the two point loads.

Applying a constant bending moment, M_z, gave calculated engineering strains with a resolution corresponding to the element mesh. However, since the material direction locally depended on the fiber orientation determined based on a single laser dot the calculated strain field contained noise. Therefore, to reduce this noise, the strain in longitudinal direction in a certain element was replaced by the average strain of the surrounding area of about 20 mm × 20 mm in the xy-plane. This filtered strain field is denoted $\boldsymbol{\varepsilon}_x(x, y, z)$. In the next step, a desired longitudinal resolution of calculated bending stiffness of the board, represented by a longitudinal distance L_r (eg 50 mm), was determined. The average longitudinal strains, $\boldsymbol{\varepsilon}_{x,r}(x_p, y, z)$, over the surrounding distance, L_r, was calculated (on the basis of $\boldsymbol{\varepsilon}_x(x, y, z)$) for positions x_p, ie longitudinal strains were calculated at every nodal position of the 5 mm mesh/grid of the cross section. Note that the distance between x_p and x_{p+1} is also 5 mm due to the chosen element grid. In clear wood sections, $\boldsymbol{\varepsilon}_{x,r}(x_p, y, z)$ is close to a linear function of y, and almost independent of z, but this is not the case in sections containing knots. $\boldsymbol{\varepsilon}_{x,r}(x_p, y, z_c)$, where z_c is a selected constant position on the z-axis, was however approximated with a linear function of y, $\bar{\varepsilon}_{x,r}(x_p, y, z_c)$, determined by linear regression performed on $\boldsymbol{\varepsilon}_{x,r}(x_p, y, z_c)$.

The cross-sectional bending stiffness of the board was finally determined based on $\bar{\varepsilon}_{x,r}(x_p, y, z_c)$, ie for a given plane of $z = z_c$, at every position x_p along the board, the cross-sectional bending stiffness was calculated as

$$EI_{z,r,c}(x_p, z_c) = \frac{M_z}{\bar{\varepsilon}_{x,r}(x_p, y_1, z_c)}(y_0 - y_1) \qquad (11)$$

where y_0 is the position on the y-axis where $\bar{\varepsilon}_{x,r}(x_p, y_0, z_c) = 0$ and y_1 is any other position along the y-axis. Thus, $EI_{z,r,c}(x_p, z_c)$ is the calculated edgewise bending stiffness, of longitudinal resolution L_r, calculated based on strains in the xy-plane where $z = z_c$. Finally, the corresponding bending MoE, $E_{b,FE}(x, z_c)$, was calculated as

$$E_{b,FE}(x, z_c) = \frac{12EI_{z,r,c}(x)}{th^3}. \qquad (12)$$

Figure 5(a) shows a calculated strain field $\boldsymbol{\varepsilon}_x(x, y, z_c)$ for $z_c = h/2$, ie the strains in longitudinal direction on one wide surface of a 600 mm long part ($6h$) of a board. Thus, the strains displayed represent average strains over surrounding areas of 20 mm × 20 mm. The inclined straight lines plotted on top of the strain plot represent $\bar{\varepsilon}_{x,r}(x_p, y_1, z_c = h/2)$, ie lines of linear regression calculated on the basis of longitudinal strains calculated across vertical sections. The distance between two adjacent lines was 5 mm, determined by the size of

the element mesh. However, the strains on which these lines are based were average strains over a distance of 50 mm, ie L_r was 50 mm. In Fig 5(b) and (c), black and red dots represent calculated average strains over the distance L_r and solid lines are lines of regression calculated based on the strains for two vertical sections of the board, one free of knots (black line in Fig 5[a] and [b]) and the other with knots (red line Fig 5[a] and [c]). In the knot free section, the black dots follow the straight line very well, with a coefficient of determination $R^2 = 0.999$, whereas in the knotty section the strain values clearly deviate from the line of regression resulting in a coefficient of determination of $R^2 = 0.915$. Figure 5(d) shows the bending MoE variation in the exhibited part of the specimen, determined for the plane $z = z_c$ based on all the lines of linear regression shown in Fig 5(a).

As explained, $E_{b,FE}(x, z_z)$ can be calculated for any value of z_c from −20 mm to 20 mm (corresponding to the full board's smaller dimension). Herein a local bending MoE of resolution L_r, representing an average over the smaller dimension of the board, is calculated as

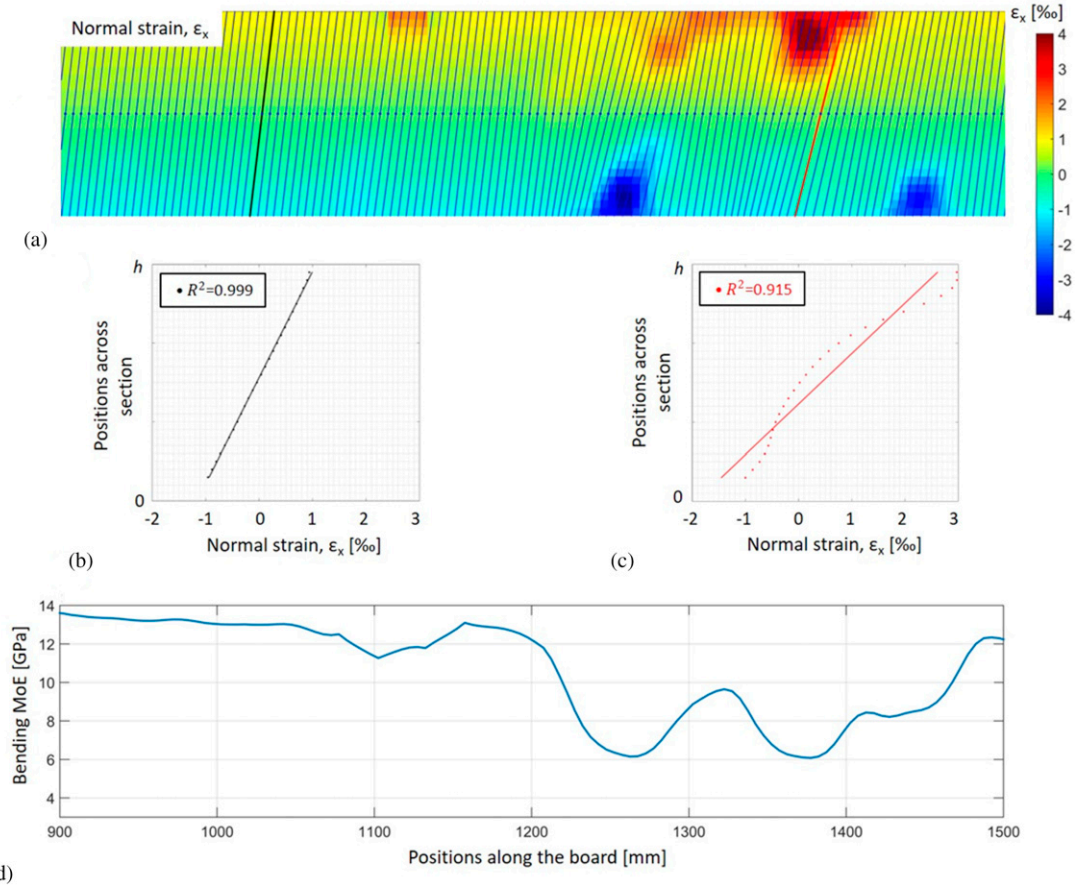

Figure 5. (a) Examples of strain distribution for a plane of $z_c = h/2$ and calculated using the FE model, where each strain value displayed represents a mean value of the surrounding area about 20 mm × 20 mm. Lines of regression of longitudinal strains across vertical cross sections are drawn on top of the strain plot. Two lines are highlighted in black and red. These are also shown in (b) and (c), respectively, along with the original strain values on which they are based. The corresponding R^2-values indicate to what extent the strains along a vertical line at a certain coordinate $z = z_c$ comply with the straight lines. (d) Bending MoE profile based on the regression lines in (a).

$$E_{\bar{b},\mathrm{FE}}(x)=\frac{1}{4}\sum_{z_c=-20;\,-5;\,5;\,20} E_{\mathrm{b,FE}}(x,z_c). \quad (13)$$

Alternative Models for Fiber Direction within Boards

In the description of the IOCS method in the "Stiffness based on integration over cross section" section, it was assumed (step a) that an in-plane fiber angle, φ, detected locally on a board surface is representative for a small area of the surface (highlighted grey area shown in Fig 4[a]) and that the fiber orientation in the interior of the board is a function of the fiber orientation on the surfaces. The original way to determine the fiber orientation in the interior of the board (Olsson et al 2013) was that φ is applied to a certain depth into the board, ie assumed valid for the sub volume $\Delta x \Delta A$ (see Fig 4[a] and [b]). This way, information from scanning of all four sides of the board is utilized but the location of the pith is not taken into account. However, location of pith determines orientation of knots, which in turn are crucial for the fiber orientation within the board. Hu et al (2018) therefore suggested an alternative model for modeling fiber orientation in the interior of boards taking location of pith into account.

Illustrations of the two alternative models for the fiber direction in the interior of the board are given in Fig 6 in which Fig 6(a) represents the original fiber angle model suggested by Olsson et al (2013), in the following referred to as fiber angle model 1 (FAM1). In this model, the fiber angle determined at a position on a board surface (red dots in Fig 6[a]) is used to represent the fiber angle in every position (shaded volume in Fig 6[a]) from the surface to a certain depth into the board (black dots in Fig 6[a]). The other model, which takes location of pith into account, is in the following referred to as fiber angle model 2 (FAM2). In this model the fiber angle in a position within the board (black dot in Fig 6[b]) is determined by the fiber angles on board surfaces at positions (red dots in Fig 6[b]) where the surfaces intersect with a straight line drawn from the pith (green dot in Fig 6[b]) through the position (black dot in Fig 6[b]) where the fiber angle shall be determined. The line intersects with two positions on board surfaces (red dots in Fig 6[b]) and the fiber angle in the position within the board (black dot in Fig 6[b]) is determined by linear interpolation of the fiber angles at the points of surface intersection. In the special case when the pith is located inside the board, the fiber direction identified in a position on the surface is used for wood between this position on the surface and the pith inside the board (constant value for all positions in the radial direction). Thus, the angle between longitudinal direction of the board and the local fibers was determined according to FAM1 and FAM2, respectively, for a set of positions, ie a 3D grid of the board volume.

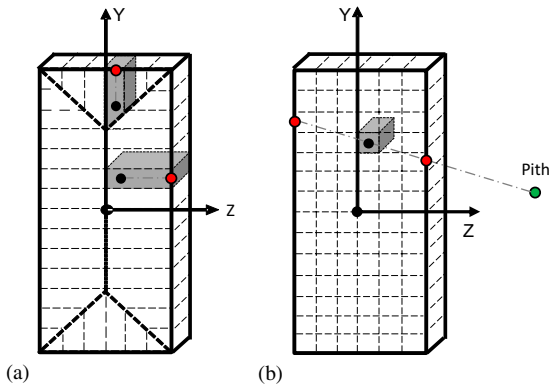

Figure 6. Models for representation, in the interior of the board, of the angle between the fiber direction and the longitudinal board direction on the basis of known such angles on the board surfaces; (a) illustration of FAM1 and (b) illustration of FAM2.

For both models the assumption is made that the longitudinal-tangential plane (*lt*-plane) of the wood material coincides with the *xy*-plane where the *x*-axis follows the longitudinal direction of the board and the *y*-axis follows the depth direction of the board, as shown in Fig 6(a) and (b). This means that the radial direction was assumed to be parallel with the *z*-direction of the board. Note that in-plane fiber angles observed on the narrow faces of the board, ie on surfaces that are actually parallel to the *xz*-plane are, nevertheless, regarded in the models as angles in the *lt*-plane. None of the FAM models is thus a complete 3D fiber orientation model (ie none of them provide a realistic

Table 1. Notation and definitions of IPs used for prediction of $E_{m,l,corr}$.

Notation of IP	Definition
$E_{500,IOCS,FAM1}$	$E_{500,IOCS,FAM1} = \frac{1}{5h} \sum_{x_s = x_c \pm 2.5h} E_b(x_s)\Delta x$, where $E_b(x)$, defined in Eq 10, is calculated using FAM1. x_c is the center position of the four-point bending test and x_s represents positions within the interval $\pm 2.5h$ where E_b is evaluated.
$E_{500,FE,FAM1}$	$E_{500,FE,FAM1} = E_{\bar{b},FE}(x_c, L_r = 5h)$ where $E_{\bar{b},FE}(x_c, L_r)$, defined in Eq 13, is calculated using FAM1.
$E_{500,IOCS,FAM2}$	$E_{500,IOCS,FAM2} = \frac{1}{5h} \sum_{x_s = x_c \pm 2.5h} E_b(x_s)\Delta x$ where $E_b(x)$ is calc. using FAM2.
$E_{500,FE,FAM2}$	$E_{500,FE,FAM2} = E_{\bar{b},FE}(x_c, L_r = 5h)$ where $E_{\bar{b},FE}(x_c, L_r)$ is calc. using FAM2.
$E_{500,IOCS,FAM1}$ & ρ_{corr}	The IP giving the highest R^2 to $E_{m,l,corr}$, combining $E_{500,IOCS,FAM1}$ and ρ_{corr} as predictor variables, in multiple linear regression.[a]
$E_{500,IOCS,FAM1}$ & $E_{a,corr}$	The IP giving the highest R^2 to $E_{m,l,corr}$, combining $E_{500,IOCS,FAM1}$ and $E_{a,corr}$ as predictor variables, in multiple linear regression.[a]
$E_{500,IOCS,FAM1}$ & $E_{a,corr}$ & ρ_{corr}	The IP giving the highest R^2 to $E_{m,l,corr}$, combining $E_{500,IOCS,FAM1}$, $E_{a,corr}$, and ρ_{corr} as predictor variables, in multiple linear regression.[a]

[a] By replacing $E_{500,IOCS,FAM1}$ with $E_{500,FE,FAM1}$, $E_{500,IOCS,FAM2}$, and $E_{500,FE,FAM2}$, respectively, corresponding IPs are obtained (with obvious notations and definitions).

distinction between radial and tangential material directions) but both provide representations of the angle between fiber direction and longitudinal board direction within the volume of the board. The advantage of FAM2, in comparison with FAM1, is that it takes the natural direction of knots, which is always from the pith and outwards, into account. As described, this is done by means of interpolation, in a direction from the pith and outwards, between two positions on different surfaces (to assign a fiber angle in a position of the interior of the board), as illustrated in Fig 6(b). Thus, FAM2 should give a more realistic representation of the angle between fibers and the longitudinal board direction of the inner of the board volume than what FAM1 does.

Definitions of Indicating Properties

It is now time to define all the IPs to be evaluated and compared with respect to their ability to predict local static MoE, $E_{m,l,corr}$, and bending strength, $f_{m,h}$, respectively. ρ_{corr} and $E_{a,corr}$, defined in Eqs 1 and 2, are often employed to predict grade determining properties. Thus, they are also included in the present evaluation, as both IPs in themselves and predictor variables in IPs that are based on several predictor variables and defined using linear regression.

In the "Models for calculation of local bending stiffness" and "Alternative models for fiber direction within boards" sections, in total four different versions of the grading method based on local bending stiffness determined based on fiber orientation from tracheid effect scanning were described, namely IOCS- and the FE-based methods (see "Stiffness based on integration over cross" and "Stiffness based on finite element method and simulation of bending" sections, respectively), used in combination with either FAM1 or FAM2 (see "Alternative models for fiber direction within boards" section). In Table 1, IPs based on the methods described, and intended for prediction of/comparison with the experimentally obtained $E_{m,l,corr}$, are defined. Correspondingly, in Table 2 IPs intended for prediction of $f_{m,h}$ are defined.

RESULTS AND DISCUSSION

Data Obtained from Laboratory Tests

In Table 3 mean values, standard deviations and coefficients of variation are presented for bending strength, density, local bending MoE and dynamic axial MoE of the 221 boards. Compared with results presented in other studies of properties of Douglas fir timber cultivated in France, strength, MoEs, and density of the present sample are all high. For example, the mean values of bending

Table 2. Notation and definitions of IPs used for prediction of $f_{m,h}$.

Notation of IP	Definition
$E_{90,IOCS,FAM1}$	$E_{90,IOCS,FAM1} = \frac{1}{0.090}\min_{p_1<x_p<p_2}\left(\sum_{x=x_p\pm0.045} E_b(x)\Delta x\right)$, where $E_b(x)$ is calculated using FAM1. p_1 and p_2 are the positions between which the local bending MoE is evaluated, ie $p_1 = x_c - 2.5h$ and $p_2 = x_c + 2.5h$, and x_p is any position between p_1 and p_2.
$E_{90,FE,FAM1}$	$E_{90,FE,FAM1} = \min_{p_1<x_p<p_2}\left(E_{\bar{b},FE}(x_p, L_r=0.090)\right)$, where $E_{\bar{b},FE}(x_c, L_r)$ is calculated using FAM1.
$E_{90,IOCS,FAM2}$	$E_{90,IOCS,FAM1} = \frac{1}{0.090}\min_{p_1<x_p<p_2}\left(\sum_{x=x_p\pm0.045} E_b(x)\Delta x\right)$, where $E_b(x)$ is calculated using FAM2.
$E_{90,FE,FAM2}$	$E_{90,FE,FAM2} = E_{\bar{b},FE}(x_c, L_r=0.090)$ where $E_{\bar{b},FE}(x_c, L_r)$ is calc. using FAM2.
$E_{90,IOCS,FAM1}$ & ρ_{corr}	The IP giving the highest R^2 to $f_{m,h}$, combining $E_{90,IOCS,FAM1}$ and ρ_{corr} in multiple linear regression.[a]
$E_{90,IOCS,FAM1}$ & $E_{a,corr}$	The IP giving the highest R^2 to $f_{m,h}$, combining $E_{90,IOCS,FAM1}$ and $E_{a,corr}$ in multiple linear regression.[a]
$E_{90,IOCS,FAM1}$ & $E_{a,corr}$ & ρ_{corr}	The IP giving the highest R^2 to $f_{m,h}$, combining $E_{90,IOCS,FAM1}$, $E_{a,corr}$, and ρ_{corr} in multiple linear regression.[a]

[a] By replacing $E_{90,IOCS,FAM1}$ with $E_{500,FE,FAM1}$, $E_{500,IOCS,FAM2}$, and $E_{500,FE,FAM2}$, respectively, corresponding IPs are obtained (with obvious notations and definitions).

strength, density, and dynamic MoE of the sample of 685 boards presented in Olsson et al (2018a) were only 34.7 MPa, 486 kg/m^3, and 11.0 GPa, respectively. The higher values of properties of the sample presented herein is explained by the fact that the boards are cut from larger logs than normal, about 50 cm in diameter, and wood at a larger distance to pith is stronger, stiffer, and of higher density than wood closer to pith (Kliger et al 1998). As expected, since the sample contains boards cut close to as well as far away from the pith, the coefficients of variation of the different properties are also significantly higher than those presented in Olsson et al (2018a).

Performance of Models and Indicating Properties

In Table 4 coefficients of determination and standard errors of estimate (SEE) among bending strength, density, local bending MoE, and axial dynamic MoE are presented. Coefficients of determination as well as SEEs are higher than the corresponding values presented in Olsson et al (2018a). For example, when $E_{a,corr}$ is the independent variable and $f_{m,corr}$ the dependent variable, R^2 and SEE are 0.54 and 12.6, respectively. Corresponding values reported in Olsson et al (2018a) are 0.47 and 8.57, respectively. Regarding the larger R^2, this is explained by the larger value range, ie larger coefficients of variation, of $E_{a,corr}$ and $f_{m,corr}$ for the current set of boards. Regarding the larger SEE, this is explained by the number and size of knots in outer wood boards. Some such boards are more or less free from knots in the constant bending moment zone (resulting in very high bending

Table 3. Mean value (mean), standard deviation (SD), and coefficient of variation (CoV) of mechanical properties, density, and MC.

	$f_{m,h}$ [MPa]	ρ_{corr} [kg/m^3]	$E_{m,l,corr}$ [GPa]	$E_{a,corr}$ [GPa]	u_s [%]
Mean	42.1	525	10.5	12.2	12.4
SD	18.5	48.7	3.59	2.96	0.83
CoV [%]	44	9	34	24	7

Table 4. Coefficient of determination and SEE between selected board properties.

	Independent variable →		$f_{m,corr}$	$E_{a,corr}$	$E_{m,l,corr}$	ρ_{corr}
Dependent variable	$f_{m,corr}$ [MPa]	R^2	1	0.54	0.68	0.32
		SEE	0	12.6	10.4	15.3
	$E_{a,corr}$ [GPa]	R^2	0.54	1	0.75	0.58
		SEE	2.01	0	1.49	1.93
	$E_{m,l,corr}$ [GPa]	R^2	0.68	0.75	1	0.43
		SEE	2.02	1.80	0	2.71
	ρ_{corr} [kg/m^3]	R^2	0.32	0.58	0.43	1
		SEE	40.2	31.8	36.8	0

Table 5. Coefficients of determination, R^2, between $E_{m,l,corr}$ and IPs as function (linear regression) of a single or a set of several predictor variables.

Independent variables utilized in linear regression	$E_{500,IOCS,FAM1}$ $E_{500,IOCS,FAM1}$ & ρ $E_{500,IOCS,FAM1}$ & $E_{a,corr}$ $E_{500,IOCS,FAM1}$ & $E_{a,corr}$ & ρ	$E_{500,FE,FAM1}$ $E_{500,FE,FAM1}$ & ρ $E_{500,FE,FAM1}$ & $E_{a,corr}$ $E_{500,FE,FAM1}$ & $E_{a,corr}$ & ρ	$E_{500,IOCS,FAM2}$ $E_{500,IOCS,FAM2}$ & ρ $E_{500,IOCS,FAM2}$ & $E_{a,corr}$ $E_{500,IOCS,FAM2}$ & $E_{a,corr}$ & ρ	$E_{500,FE,FAM2}$ $E_{500,FE,FAM2}$ & ρ $E_{500,FE,FAM2}$ & $E_{a,corr}$ $E_{500,FE,FAM2}$ & $E_{a,corr}$ & ρ
R^2 to $E_{m,l,corr}$	0.62	0.70	0.65	0.70
	0.72	0.79	0.75	0.80
	0.81	0.84	0.82	0.84
	0.81	0.84	0.82	0.84

strength) while others may have a single very large knot in this critical zone (resulting in very low strength). However, the difference in axial dynamic MoE may be comparatively small, which results in larger prediction errors.

In Table 5, coefficient of determination among local bending MoE, $E_{m,l,corr}$, and IPs is presented, the latter based on a single or a set of independent variables as described and defined in Table 1. Thus each column in this table represents one of the four different model combinations (IOCS or FEM in combination with FAM1 or FAM2) for calculation of local bending MoE over a span of $5h$ (500 mm). Comparing first the performance of the single independent variables $E_{500,IOCS,FAM1}$, $E_{500,FE,FAM1}$, $E_{500,IOCS,FAM2}$, and $E_{500,FE,FAM2}$, it is shown, as expected, that the FE model enables better prediction of local MoE than what the simpler IOCS model does, with R^2 of 0.70 using the FE model (FAM1 or FAM2 give the same R^2) and 0.62 and 0.65 using the IOCS model (in combination with FAM1 and FAM2, respectively). Comparing next the increase of coefficients of determination when adding ρ or $E_{a,corr}$ as additional independent variables to $E_{m,l,corr}$, any of them contribute to raise the coefficient of determination. $E_{a,corr}$ gives larger improvement than what ρ does. Combined use of $E_{a,corr}$ and $E_{500,FE,FAM1}$ (or $E_{500,FE,FAM2}$) gives an R^2 to $E_{m,l,corr}$ as high as 0.84. Adding ρ as a third independent variable does not give further improvement.

In Table 6 coefficients of determination between $f_{m,corr}$ and IPs are presented. Here, the independent variables based on the four models (IOCS or FEM in combination with FAM1 or FAM2) represent local bending MoE over spans of only 90 mm, rather than over 500 mm as is the case for the predictor variables used Table 5. Comparison of performance of the four alternative models, represented by $E_{90,IOCS,FAM1}$, $E_{90,FE,FAM1}$, $E_{90,IOCS,FAM2}$, and $E_{90,FE,FAM2}$, respectively, to predict $f_{m,corr}$ leads to similar conclusions as regarding prediction of $E_{m,l,corr}$ in the sense that the FE model gives more accurate prediction of $f_{m,corr}$ than what the IOCS model does, even though the improvement of using the FE model is not quite as large as for prediction of $E_{m,l,corr}$. However, results shown in Table 6 indicate that FAM2 give better prediction of $f_{m,corr}$ than what FAM1 does and, consequently, the highest coefficient of determination

Table 6. Coefficients of determination R^2 between $f_{m,corr}$ and IPs as function (linear regression) of a single or a set of several predictor variables.

Independent variables utilized in linear regression	$E_{90,IOCS,FAM1}$ $E_{90,IOCS,FAM1}$ & ρ $E_{90,IOCS,FAM1}$ & $E_{a,corr}$ $E_{90,IOCS,FAM1}$ & $E_{a,corr}$ & ρ $E_{a,corr}$ & ρ	$E_{90,FE,FAM1}$ $E_{90,FE,FAM1}$ & ρ $E_{90,FE,FAM1}$ & $E_{a,corr}$ $E_{90,FE,FAM1}$ & $E_{a,corr}$ & ρ	$E_{90,IOCS,FAM2}$ $E_{90,IOCS,FAM2}$ & ρ $E_{90,IOCS,FAM2}$ & $E_{a,corr}$ $E_{90,IOCS,FAM2}$ & $E_{a,corr}$ & ρ	$E_{90,FE,FAM2}$ $E_{90,FE,FAM2}$ & ρ $E_{90,FE,FAM2}$ & $E_{a,corr}$ $E_{90,FE,FAM2}$ & $E_{a,corr}$ & ρ
R^2 to $f_{m,corr}$	0.61	0.65	0.64	0.68
	0.70	0.72	0.73	0.75
	0.70	0.72	0.72	0.74
	0.71	0.73	0.74	0.76
	0.54	—	—	—

using a single independent variable is obtained for $E_{90,FE,FAM2}$, for which $R^2 = 0.68$. Adding ρ or $E_{a,corr}$ as a second independent variable to predict $f_{m,corr}$ means considerable improvement. It is interesting to note that ρ gave at least as large improvement to the coefficient of determination as what $E_{a,corr}$ did. However, for other samples of Douglas fir and Norway spruce (Olsson et al 2018a) $f_{m,corr}$ was more accurately predicted using [$E_{90,IOCS,FAM1}$ & $E_{a,corr}$] than using [$E_{90,IOCS,FAM1}$ & ρ].

In Fig 7(a) graphical illustration is given of some of the results presented in Table 6. In Fig 7(a), the scatter plot and linear regression line between $f_{m,corr}$ and [$E_{90,IOCS,FAM1}$ & $E_{a,corr}$ & ρ] with $R^2 = 0.71$ and SEE = 10.0 MPa is shown. This IP is similar to the original one first suggested by Olsson et al (2013) which was also based on IOCS and FAM1 (although in the present study, only the part of the board of length 5h, centered between the point loads in the destructive test is actually considered. See the definition given in Table 1). In Fig 7(b), the scatter plot between $f_{m,corr}$ and [$E_{90,FE,FAM2}$ & $E_{a,corr}$ & ρ] with $R^2 = 0.76$ and SEE = 9.2 MPa is shown, and in Fig 7(c) the scatter plot between $f_{m,corr}$ and $E_{a,corr}$ with $R^2 = 0.54$ and SEE = 12.6 MPa. The histogram in Fig 7(d) shows the errors of estimated modulus

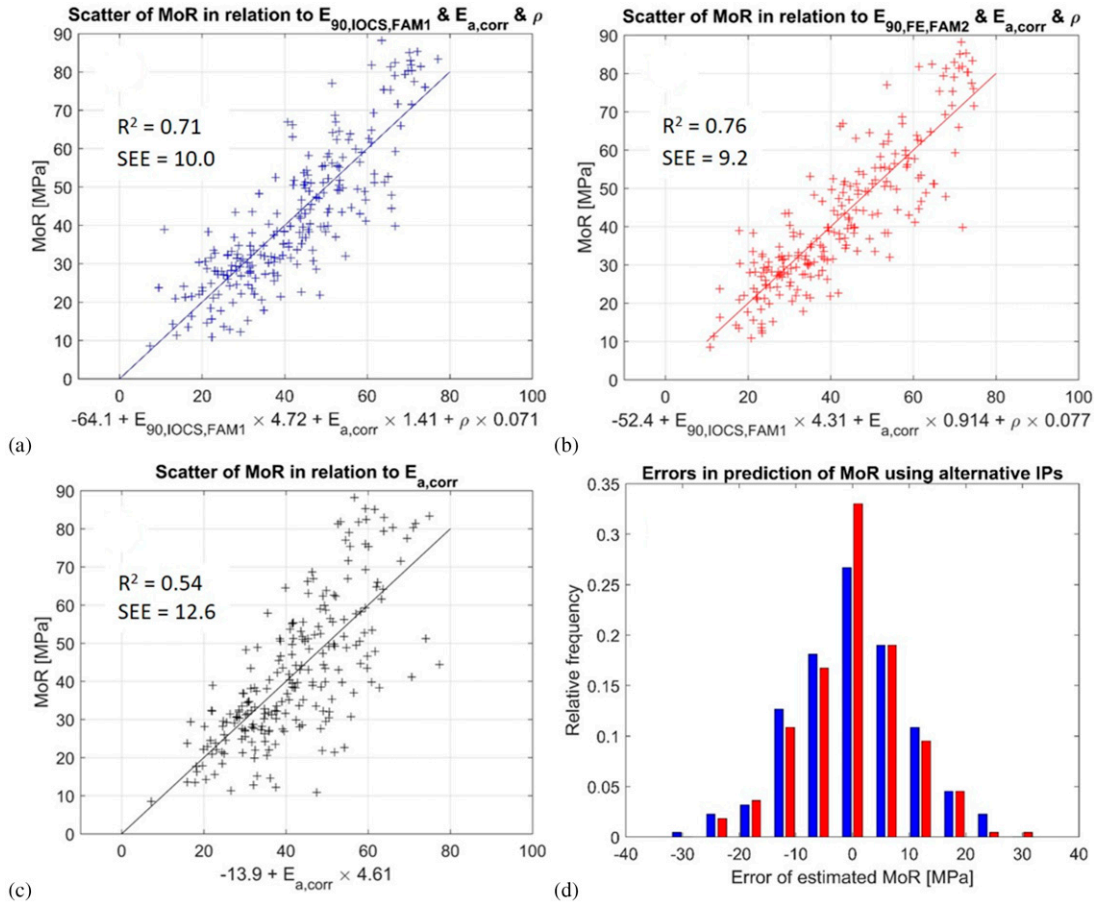

Figure 7. Selected results of relationships between IPs and MoR ($f_{m,corr}$); (a-c) scatter plots and results of linear regression of [$E_{90,IOCS,FAM1}$ & $E_{a,corr}$ & ρ], [$E_{90,FE,FAM2}$ & $E_{a,corr}$ & ρ], and $E_{a,corr}$, respectively, to MoR and (d) histogram of errors of estimated MoR using as IP [$E_{90,IOCS,FAM1}$ & $E_{a,corr}$ & ρ] (blue bars) and [$E_{90,FE,FAM2}$ & $E_{a,corr}$ & ρ] (red bars).

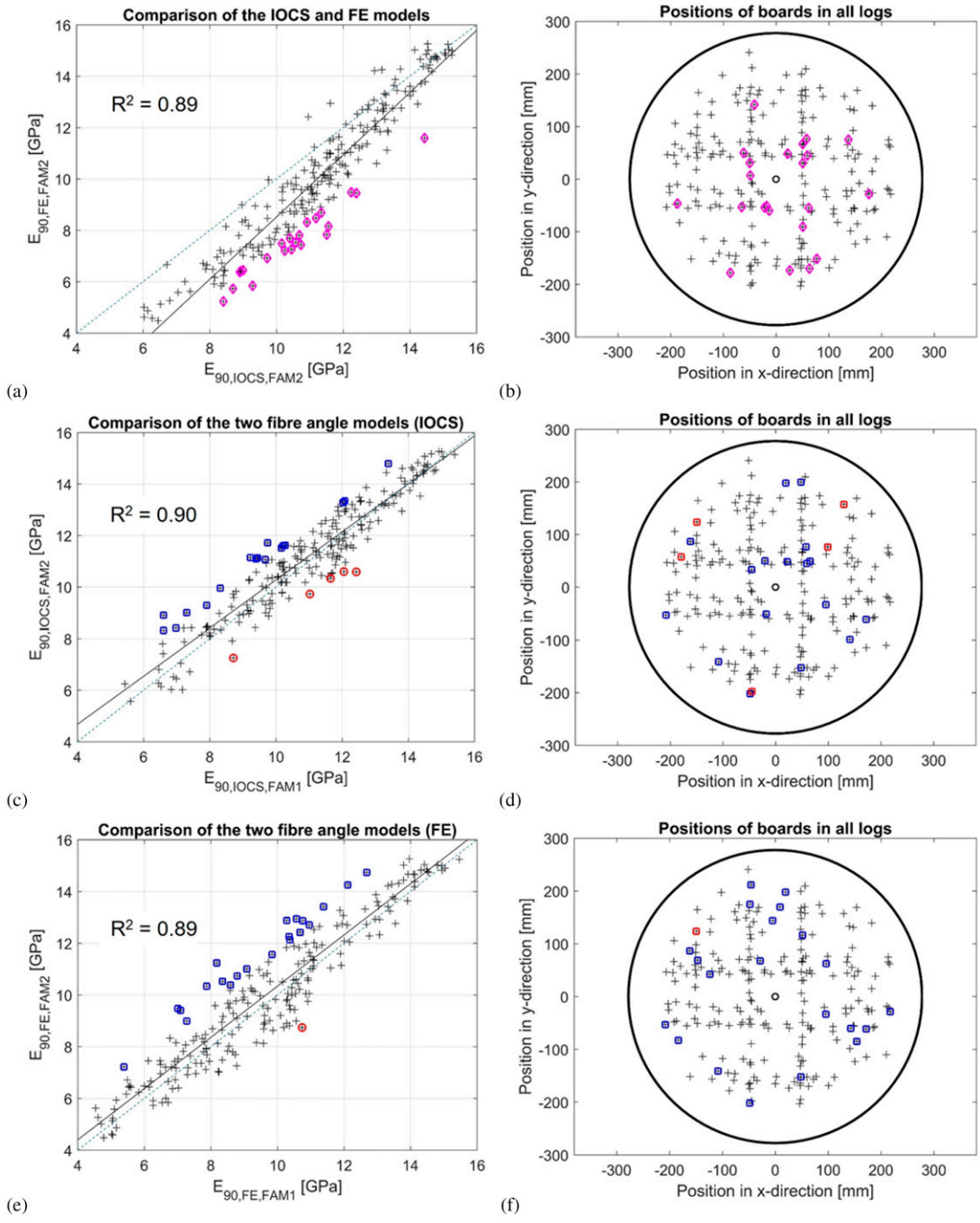

Figure 8. Relationships between calculated local bending stiffness using the IOCS and the FE models, and using FAM1 and FAM2, along with positions of highlighted boards in relation to pith of the log; (a and b) $E_{90,FE,FAM2}$ vs $E_{90,IOCS,FAM2}$; (c and d) $E_{90,IOCS,FAM2}$ vs $E_{90,IOCS,FAM1}$; (e and f) $E_{90,FE,FAM2}$ vs $E_{90,FE,FAM1}$.

of rupture (MoR) using [$E_{90,IOCS,FAM1}$ & $E_{a,corr}$ & ρ] (bars in blue) and [$E_{90,FE,FAM2}$ & $E_{a,corr}$ & ρ] (bars in red), where the latter shows a noticeable improvement compared with the former.

Some further analysis of the differences between IOCS and FE models, and between FAM1 and FAM2 follows. In Fig 8(a), a scatter plot between the predictors $E_{90,IOCS,FAM2}$ and $E_{90,FE,FAM2}$ is shown. The 10% of the boards with largest values of $|E_{90,IOCS,FAM2}-E_{90,FE,FAM2}|$ are highlighted (magenta diamonds). The solid line through the scatter plot is the linear regression line and the dashed line is given by $y = x$. As expected, the FE model (represented by $E_{90,FE,FAM2}$) gives, for most the boards, a lower calculated bending stiffness than what the IOCS model (represented by $E_{90,IOCS,FAM2}$) does. This is because the IOCS model tends to overestimate the bending stiffness as explained in the "Stiffness based on integration over cross section" section. The very idea of replacing IOCS with FE was to resolve this. For a few boards, however, especially boards with high calculated bending stiffness, the FE model gives slightly higher stiffness than what the IOCS model does. This is because the FE mesh and the linear elements used give a somewhat too high bending stiffness. Thus, the conclusion drawn from an introductory convergence study (see "Stiffness based on finite element method and simulation of bending" section and Hu et al 2018) was not quite accurate. With a finer element mesh and/or use of higher order elements, the FE model would not give higher stiffness than the IOCS model for any of the boards. In Fig 8(b) the position of the center of each board's end cross section, in relation to the pith of the log from which it is cut, is indicated. Just as in Fig 8(a), the boards with largest values of $|E_{90,IOCS,FAM2}-E_{90,FE,FAM2}|$ are highlighted (magenta diamonds) and it can be seen in Fig 8(b) that most of these boards are located closer to pith than the average board of the sample. Closer to pith it is more common 1) that several knots are located close to each other and therefore may have an influence on the bending stiffness of the 90 mm long section along the board for which the bending stiffness is calculated, and 2) that knots are not directed in a 90 degree angle to the direction of the board, since the angle between the direction of a certain branch/knot and the direction of the tree is smaller for the younger tree than for the older tree. For these reasons, the FE model was expected to result in lower bending stiffness particularly for boards cut close to the pith, and this is precisely what is indicated by the results shown in Fig 8(a) and (b). For a sample of boards cut from smaller logs it is likely that the difference of results, comparing $E_{90,IOCS,FAM2}$ with $E_{90,FE,FAM2}$, would be larger, rather than smaller, since then a higher proportion of the boards would be located close to the pith.

In Fig 8(c) and (e), scatter plots between $E_{90,IOCS,FAM1}$ and $E_{90,IOCS,FAM2}$, and between $E_{90,FE,FAM1}$ and $E_{90,FE,FAM2}$, are shown. Thus, both plots represent comparisons between FAM1 and FAM2. The 10% of the boards with largest difference of calculated bending stiffness using FAM1 and FAM2, ie largest values of $|E_{90,IOCS,FAM1}-E_{90,IOCS,FAM2}|$ and $|E_{90,FE,FAM1}-E_{90,FE,FAM2}|$ are highlighted (blue squares when FAM2 gives higher stiffness and red circles when FAM1 gives higher stiffness). For most of the highlighted boards (boards with the largest difference in stiffness) FAM2 gives the higher stiffness. In Fig 8(d) and (f), the positions of the boards in relation to pith of the log are shown. No very clear pattern is, however, identified regarding the position of the cross sections of highlighted boards in relation to the pith.

CONCLUSIONS AND FURTHER WORK

Two different potential improvements of a method to predict bending strength of sawn timber were evaluated herein using a relatively large sample of Douglas fir boards. The improvements consists of 1) the use a 3D FE model, rather than a model based on simple IOCSs, to calculate the local bending MoE over weak section of length 90 mm in longitudinal board direction and 2) a more realistic model of the local angle between wood fibers and longitudinal board direction in the interior of boards, taking location of pith and directions of knots into account.

Results show that the use of the 3D FE model, rather than the simpler IOCS model, allows for more accurate prediction of bending stiffness. For prediction of the local bending MoE over five times the larger board dimension, $E_{m,l,corr}$, the coefficient of determination increased from $R^2 = 0.62$ to $R^2 = 0.70$ when using data from fiber orientation measurements alone, and from $R^2 = 0.81$ to $R^2 = 0.84$ when based on data of fiber orientation in combination with data of board resonance frequency and density. For prediction of bending strength, $f_{m,corr}$, the coefficient of determination increased from $R^2 = 0.61$ to $R^2 = 0.65$ when using data from fiber orientation measurements alone, and from $R^2 = 0.71$ to $R^2 = 0.73$ when based on data of fiber orientation, resonance frequency and density. Thus, the results indicate that the use of a 3D FE model, rather than simple IOCS, for calculation of local bending MoE as IP to bending strength gives an improvement. The employed FE model is quite simple and with suitable implementation in computer code, it would be possible to use it for grading in production speed.

The use of the more advanced model for fiber angles of the interior of the board did not contribute significantly to increased accuracy in prediction of $E_{m,l,corr}$. When using data from fiber orientation in combination with data of resonance frequency and density, about the same accuracy was obtained no matter if FAM1 or FAM2 was used ($R^2 = 0.81$ and 0.82, respectively using IOCS, and $R^2 = 0.84$ using FE). For prediction of $f_{m,corr}$, however, the coefficient of determination increased from $R^2 = 0.61$ to $R^2 = 0.64$ when using data from fiber orientation measurements alone, and from $R^2 = 0.71$ to $R^2 = 0.74$ (using IOCS) and from $R^2 = 0.73$ to $R^2 = 0.76$ (using FE) when based on data of fiber orientation, resonance frequency and density. It should be noted, however, that application of the improved fiber angle model requires knowledge of approximate location of pith for each board assessed. In this study such knowledge was obtained manually, on one end of the boards. However, it has recently been shown that location of pith can be determined automatically, in very high speed and with high resolution along the board (Habite et al 2022).

Combining the 3D FE model with the improved fiber angle model (FAM2) was quite successful and gave a coefficient of determination to $f_{m,corr}$ as high as $R^2 = 0.76$. Thus, altogether, an increase in coefficient of determination of about 0.05 was achieved. This represents a considerable improvement of the original IP and grading method first proposed by Olsson et al (2013).

The basic idea behind the machine strength grading method discussed herein is to calculate a local bending MoE over a short length of only about 90 mm, and that this correlates strongly to bending strength. The work presented herein contributes to more accurate determination of such local bending MoE. The herein suggested model for fiber angle in the interior of the board still represents a considerable simplification of the true 3D fiber orientation and it is possible that further improvements of the fiber orientation model may contribute to further increase of grading accuracy using the evaluated method. However, the accuracy obtained herein ($R^2 = 0.76$ between IP and $f_{m,corr}$) may be close to what can be achieved using this concept.

Further development toward more accurate grading than what has been achieved herein may require either some new, complementary predictor variable, one that is not strongly correlated with those employed herein, or a model of the board by which strength can be calculated in a more direct way, ie not only via calculation of local bending MoE. It is, however, likely that such calculation of strength would require a model of the fiber orientation around knots that is more accurate than the one employed herein. Thus, development of such models is yet another subject for further research and development in this field.

ACKNOWLEDGMENTS

This research was made possible through financial support of the Bourgogne Franche-Comté regional council and the French National Research Agency (ANR) in the framework of the TreeTrace project, ANR-17-CE10-0016.

REFERENCES

Bacher M (2008) Comparison of different machine strength grading principles. *in* Proceedings, 2nd Conference

COST Action E53—Quality Control for Wood and Wood Products, October 29-30, Delft, the Netherlands.

Briggert A, Hu M, Olsson A, Oscarsson J (2018) Tracheid effect scanning and evaluation of in-plane and out-of-plane fiber direction in Norway spruce using. Wood Fiber Sci 50(4):411-429.

Briggert A, Olsson A, Oscarsson J (2020) Prediction of tensile strength of sawn timber: Definitions and performance of indicating properties based on surface laser scanning and dynamic excitation. Mater Struct 53(54):1-20.

Daval V, Pot G, Belkacemi M, Meriaudeau F, Collet R (2015) Automatic measurement of wood fiber orientation and knot detection using an optical system based on heating conduction. Opt Express 23:33529-33539.

EN 384 (2016). Structural timber—Determination of characteristics values of mechanical properties and density. European Committee for Standardization.

EN 408 (2010) + A1 (2012). Timber structures—Structural timber and glued laminated timber—Determination of some physical and mechanical properties. European Committee for Standardization.

EN 14081-2 (2018). Timber structures—Strength graded structural timber with rectangular cross section—Part 2: Machine grading; additional requirements for type testing. European Committee for Standardization.

Foley C (2003) Modeling the effects of knots in structural timber. Doctoral thesis, Report TVBK-1027, Lund Inst of Technol, Lund, Sweden.

Habite T, Abdeljaber O, Olsson A (2021) Automatic detection of annual rings and pith location along Norway spruce timber boards using conditional adversarial networks. Wood Sci Technol 55:461-488.

Habite T, Abdeljaber O, Olsson A. (2022) Determination of pith location along Norway spruce timber boards using one dimensional convolutional neural networks trained on virtual timber boards. Constr Build Mater 329:127129. https://doi-org.proxy.lnu.se/10.1016/j.conbuildmat.2022.127129

Habite T, Abdeljaber O, Oscarsson J (2020) Automatic detection of pith location along Norway spruce timber boards on the basis of optical scanning. Eur J Wood Wood Prod 78:1061-1074. https://doi-org.proxy.lnu.se/10.1007/s00107-020-01558-1

Hanhijärvi A, Ranta-Maunus A (2008) Development of strength grading of timber using combined measurement techniques. Report of the Combigrade-Project—Phase 2. VTT Publications 686.

Hu M, Olsson A, Johansson M, Oscarsson J (2018) Modelling local bending stiffness based on fiber orientation in sawn timber. Eur J Wood Wood Prod 76(6): 1605-1621.

Jenkel C, Kaliske M (2018) Simulation of failure in timber with structural inhomogeneities using an automated FE analysis. Comput Struct 207:19-36. https://doi-org.proxy.lnu.se/10.1016/j.compstruc.2017.11.016

Kandler G, Lukacevic M, Füssl J (2016) An algorithm for the geometric reconstruction of knots within timber boards based on fiber angle measurements. Constr Build Mater 124:945-960. https://doi-org.proxy.lnu.se/10.1016/j.conbuildmat.2016.08.001

Kliger R, Perstorper M, Johansson G (1998) Bending properties of Norway spruce timber. Comparison between fast- and slow-grown stands and influence of radial position of sawn timber. Ann Sci 55(3):349-358. https://hal.archives-ouvertes.fr/hal-00883206

Lukacevic M, Füssl J, Eberhardsteiner J (2015) Discussion of common and new indicating properties for the strength grading of wooden boards. Wood Sci Technol 49(3):551-576. https://doi-org.proxy.lnu.se/10.1007/s00226-015-0712-1

Lukacevic M, Kandler G, Hu M, Olsson A, Füssl J (2019) A 3D model for knots and related fiber deviations in sawn timber for prediction of mechanical properties of boards. Mater Des 166:1-18. https://doi-org.proxy.lnu.se/10.1016/j.matdes.2019.107617

Matthews P, Beech B (1976) Method and apparatus for detecting timber defects. U.S. Patent 3976384.

Nocetti M, Bacher M, Brunetti M, Crivellaro A, van de Kuilen JWG (2010) Machine grading of Italian structural timber: Preliminary results on different wood species. *in* Proceedings, 11th World Conference on Timber Engineering, June 20-24, Riva del Garda, Italy.

Olsson A, Oscarsson J (2017) Strength grading on the basis of high resolution laser scanning and dynamic excitation: A full scale investigation of performance. Eur J Wood Wood Prod 75:17-31. https://doi-org.proxy.lnu.se/10.1007/s00107-016-1102-6

Olsson A, Oscarsson J, Serrano E, Källsner B, Johansson M, Enquist B (2013) Prediction of timber bending strength and in-member cross-sectional stiffness variation on the basis of local wood fiber orientation. Eur J Wood Wood Prod 71(3):319-333. https://doi-org.proxy.lnu.se/10.1007/s00107-013-0684-5

Olsson A, Pot G, Viguier J, Faydi Y, Oscarsson J (2018a) Performance of strength grading methods based on fiber orientation and axial resonance frequency applied to Norway spruce (*Picea abies* L.), Douglas fir (*Pseudotsuga menziesii* (Mirb.) Franco) and European oak (*Quercus petraea* (Matt.) Liebl./*Quercus robur* L.). Ann Sci 75(102):1-18. https://doi-org.proxy.lnu.se/10.1007/s13595-018-0781-z

Olsson A, Serrano E, Oscarsson J, Enquist B, Johansson M, Källsner B (2018b) Method and device for evaluating a wooden board. US 9,863,929 B2.

Oscarsson J (2014) Strength grading of structural timber and EWP laminations of Norway spruce—Development potentials and industrial applications, Report no. 170/2014, Linnaeus University, Växjö, Sweden.

Sarnaghi AK, van de Kuilen JWG (2019) An advanced virtual grading method for wood based on surface information of knots. Wood Sci Technol 53:535-557. https://doi-org.proxy.lnu.se/10.1007/s00226-019-01089-w

Soest J, Matthews P, Wilson B (1993) A simple optical scanner for grain defects. *in* Proceeding, 5th Int Conference Scanning Technologies & Process Control for the Wood Prod Industry, October 25-27, Atlanta, GA.

Viguier J, Bourreau D, Bocquet JF, Pot G, Bléron L, Lanvin JD (2017) Modelling mechanical properties of spruce and Douglas fir timber by means of X-ray and grain angle measurements for strength grading purpose. Eur J Wood Wood Prod 75(4):527-541.

Wright S, Dahlen J, Montes C, Eberhart T (2019) Quantifying knots by image analysis and modeling their effects on the mechanical properties of loblolly pine lumber. Eur J Wood Wood Prod 77:903-917. https://doi-org.proxy.lnu.se/10.1007/s00107-019-01441-8

INVESTIGATION OF BIOGAS DIGESTATE AS FIBER MATERIALS FOR COMPOSITES

*Marion Gebhardt**

Researcher
German Institutes of Textile and Fibre Research
Koerschtalsstraße 26, 73770 Denkendorf, Germany
E-mail: marion.luetz@uni-hohenheim.de

Andreas Lemmer

Researcher, Deputy Director
State Institute of Agricultural Engineering and Bioenergy
University of Hohenheim
Garbenstraße 9, 70599 Stuttgart, Germany
E-mail: andreas.lemmer@uni-hohenheim.de

(Received October 2022)

Abstract. Fiber reinforced plastics with synthetic fibers are widely used. Plant fibers are also known to produce more sustainable composites. However, there is a great interest in finding alternatives to classical natural fibers. The digestate of biogas plants seems to be such an alternative. Biogas plants are fed with plant-based substrates and during the digestion, the biomass is degraded. In this study, the fiber quality of digestates from four biogas plants with different initial substrates is investigated. Therefore, typical fiber properties, such as slenderness ratio, cell wall components, and the potential fiber performance, are measured. According to the general definition, the solid part of the digestate is a fiber material. The slenderness ratio is 5 or higher and the density is 1.5 gcm^{-3}, which is typical for natural fibers. Fibers with similar properties are already used in composite materials.

Keywords: Bio composites, waste material, natural fibers, biorefinery.

INTRODUCTION

Fiber-based composites with different reinforcing fibers are used in various industries. Fiber-reinforced composites typically consist of a reinforcing fiber component, which absorbs the forces, and a matrix, which gives the shape and protects the fibers from environmental influences. In general, fibers are defined as thin filamentary structures (Crowther 1995) that have a slenderness ratio (length/diameter) of at least 3:1 (Schenek 2001). It is possible to mix individual short (1-10 mm), long (smaller than 25 mm), or continuous fibers with the polymer matrix. Fibers are often processed into reinforcing textiles (eg nonwovens, woven, or tailored fabrics) (Schürmann 2007). Fibers for textile applications have a very large slenderness ratio of 1000:1 and more (Schenek 2001). The requirements for nonwoven technology are fibers with a length of up to 5-30 mm, which must not be too slender. Very short fibers are often processed as fillers in thermoplastics, for example, in wood plastic composites (WPC), where wood flour and wood fibers are common (Vogt 2006; Schürmann 2007). The scarcity of resources and the goal of reducing the high energy consumption in the production of many composites are forcing the industry to use alternatives. Natural fibers, especially plant fibers such as flax, are often used to produce sustainable composites. The density of plant fibers is typically approximately 1.5 gcm^{-3} (Schenek 2001) and their specific (density-related) properties are comparable to those of glass fibers (AVK 2013; Salit et al 2015). Plant fibers must be extracted from plants by biological, chemical, or sometimes, mechanical methods. This causes additional process steps and energy consumption (Gessner 1955; Ahmed and Akhter 2001). Plant fibers are grown on agricultural land that cannot be used for feed or food production. Various fiber

* Corresponding author

crops are grown around the world. For example, 264152ha of flax and 82265ha of hemp were harvested in 2019 (FAO 2021). Fiber yield varies due to weather conditions and crop varieties (Riedel and Nickel 2000). In 2019, the global flax fiber yield was 4.2tha−1, whereas yield of hemp and sisal fibers was both 2.5tha−1 (FAO 2021). As a lignocellulosic material, plant fibers are mainly composed of the cell wall materials cellulose, lignin, and hemicellulose. To save land and energy, it is interesting to find other fiber sources. Fibrous residues are sometimes used in short fiber-reinforced plastics or filled plastics. An example of residue use is fibers from coconut production in nonwovens for composites (Sergion et al 2005; Bradley and Conroy 2019; Obeng et al 2020). Another example is fibers or wood flour from sawmill by-products of the wood industry in thermoplastic WPC and derived timber products (Sörgel et al 2006; Vogt 2006). Cellulose and lignin content and length of selected plant fibers and agricultural waste materials are shown in Table 1.

Digestate from biogas plants is mostly used as fertilizer. In Germany, industry is urged to use more sustainable raw materials to achieve the goal of a bioeconomy (BMBF 2020). Digestate can be a solution for fiber and composite production. Due to the lignocellulosic components, digestate can be an interesting raw material for industrial purposes. Essel et al (2015) mixed small amounts of purified and treated digestate into the production process of medium-density fiberboard. An addition of 20% digestate does not influence the mechanical properties, a higher addition leads to a decrease. In another study, digestate was added to various plastic products, such as films, to reduce weight and increase biodegradability (König and Fudel 2005).

Biogas technology is used worldwide to generate renewable energy through anaerobic microbial conversion of substrates fed to the digesters of these plants. Approximately, 132,000 technical-scale plants are currently in operation worldwide. In addition, the number of small-scale household biogas plants installed is estimated to be in the millions (Jain 2019). In Europe, there are currently approximately 17,000 biogas plants, of which 10,000 are located in Germany (Königsberger et al 2019). In Germany, the most commonly used substrates for biogas plants are manure from livestock with 12% of the substrates (dry mass 12%) and energy crops with 79% (dry mass 17-32%), with corn silage accounting for the largest share (Foreest 2012; Torrijos 2016; Daniel-Gromke et al 2017; Scarlat et al 2018). The anaerobic degradability of substrates and their conversion rate into biogas is mainly influenced by the proportion of cell wall components and their water content. In contrast to the cell contents, the lignocellulose complexes of the cell walls can only be degraded to a small extent under the anaerobic conditions of the biogas process and are found as fibrous materials in the aqueous suspension of the fermentation residues (digestate) together with the minerals

Table 1. Cellulose and lignin content of different plants related to dry mass from Fortea-Verdejo et al (2017), Garrote et al (1999), Ververis et al (2003), Obeng et al (2020), Bradley and Conroy (2019) Nielsen (2005), Tiefenthaller (2006).

Fibrous part of the plant or waste material	Cellulose (%)	Lignin (%)	Fiber length (mm)	Dry mass (%)	Dry mass after digestion (%)
Cotton	90	NN	12-64	—	—
Flax	70	2	3-4	—	—
Softwood	42	29	4	—	—
Hardwood	41	19	1	—	—
Coconut husk	—	41-46	—	—	—
Grass silage	34	9	—	—	—
Corn silage	21	7	—	32	11
Cattle slurry	15-25	7-9	—	8	6
Pig Slurry	10-23	4-10	—	6	4
Solid manure	13	17	—	25	15

(Schimpf 2014). Undegraded fiber materials from the digestate of biogas plants are potentially suitable for the production of composite materials. During anaerobic digestion, the biomass is partially degraded and the fibers are released, which corresponds to the typical biological extraction processes for fiber production. If the solids of the digestate are used for the production of fiber composites, the added value of biogas production can be increased. The biogas plant can be a kind of biorefinery because energy and industrial raw materials are produced. The fibers of the digestate are potentially very interesting raw materials for industrial use, as they can be produced in large quantities at low cost and with low energy input. So far, little is known about the quantity and quality of extractable fibers from digestate. The aim of this work is, therefore, to evaluate the influence of different initial substrates on fiber quantity and quality.

MATERIALS AND METHODS

Samples are taken from four economically operating biogas plants in southern Germany (hereafter referred to as A, B, C, and D). The samples were taken from the three process steps: the fermenter (F1), the secondary fermenter (F2), and the storage tank (ST). A questionnaire was used to obtain further information about the biogas plant and the quantities of substrates processed. For initial characterization, the extracted fibrous materials were analysed using the van Soest analysis (Van Soest and Robertson 1970) based on DIN EN ISO 13906 and 16472 (DIN 2006, 2008). Before analysis, the digestate was ground to powder with a cutting mill. The different cell wall components were determined in three steps. To obtain neutral detergent fiber (NDF), all components that do not belong to the cell wall were washed out with a so-called neutral detergent solution. For the so-called acid detergent fiber (ADF), the cell wall components, except lignin and cellulose, were removed by boiling for 1 h in acid detergent solution. To obtain the so-called acid detergent lignin (ADL), cellulose was removed by exposure to 72% sulfuric acid for 3 h. After all three steps, the samples were washed with hot water to remove the solutes and dried at 105°C. After performing the dissolution steps, the remaining material was burned at 500°C to obtain the ash content. The proportions of the solution fractions (NDF/ADF/ADL) were calculated using the mass of the dried material m_{dry}, the mass of the fresh material m_{fresh}, and the mass of the ash after burning mash with Eq (1).

$$NDF/ADL/ADL\% = ((m_{dry}–m_{ash})/m_{dryfresh}) * 100. \quad (1)$$

The exact content of cellulose, hemicellulose, and lignin were determined by subtracting the individual percentages (see Eqs 2-5). The amount of each component is given as a ratio of dry mass (Schuldt and Dinse 2010).

$$\text{soluble}\% = 100\% - \text{NDF}\%. \quad (2)$$

$$\text{hemicellulose}\% = \text{NDF}\% - \text{ADF}\%. \quad (3)$$

$$\text{cellulose}\% = \text{ADF}\% - \text{ADL}\%. \quad (4)$$

$$\text{lignin}\% = \text{ADL}\% - \text{ash}\%. \quad (5)$$

The dry mass content was determined according to DIN 12880 and DIN 12879. For the determination, a quantity of the respective fermentation residue was weighed and dried at 100°C until no further mass loss was detected and then weighed again (Pfeiffer and Thrän 2015). Eq (6) was used to calculate the dry mass content.

$$DM\% = \frac{m_{dry}}{m_{fresh}} * 100. \quad (6)$$

To avoid errors related to cavities in the fiber material, the dried digestate was compacted and formed into flat tablets of 10-mm diameter at a pressure of approximately 10 bar. The density measurement was carried out according to EN ISO 1183-2. Instead of a density column, a row of density mixtures with *n*-heptane (0.68 gcm^{-3}), carbon tetrachloride (1.59 gcm^{-3}), and 1,3 dibromopropane (1.99 gcm^{-3}) was prepared in different beakers. The fermentation residue pills were immersed in the solvent mixtures one after the other until a floating state was reached. At this point, both materials have the same density (DIN 2004).

Fiber length was determined for all digestates according to DIN 53808-1 (Saville 1999). First, a sample of each of the digestates was placed in a glass dish and scanned. On the resulting image, all the individual fibers of each sample were traced and measured using an image processing program (Rueden et al 2017). This way, approximately 1000 individual measurements were taken from each sample. In addition to the fiber length, the slenderness ratio is also an important parameter. To determine this ratio, the fiber diameter must first be determined. The shapes of the digestate are very irregular and do not have a uniform round cross section. To obtain an approximate value for the slenderness ratio, the width of the fibers was measured directly from the scans. This determination was carried out on 100 individual fibers of each sample. Using wet sieve analysis according to DIN 66165, the samples were allocated and classified according to their size (Fritsch, analysette3, Idar-Oberstein, Germany). In this way, the proportion of potentially processable fibers was determined. Sieving was performed with water and vibration (amplitude 2 mm) at cycles of 10 min.

The sieves had a mesh size of 2, 1, 0.5, 0.25, and 0.125 mm, and were stacked in descending order. Each sample was placed on the coarsest sieve and then sprinkled with water. The sample material remaining on the sieves was rinsed, filtered, and dried. To determine the proportions of each size class, the filtration residues are weighed (Schmidt et al 2003).

RESULTS AND DISCUSSION

Description of Biogas Plants and Used Substrates

All four biogas plants investigated are located in southern Germany. In biogas plant A, the gas is purified and fed into the public gas grid. In plants B, C, and D, the gas is used in a combined heat and power plant (CHP) to generate electricity. In all four selected biogas plants, mainly agricultural materials are used as substrates. The input substrates with the corresponding quantity shares of the investigated biogas plants are shown in Table 2. The collected samples and data represent for only 1 mo of the year. Plant A uses only plant substrates, with chopped hop vines making up the largest portion. Plant B uses cereal whole-plant silage and manure as main substrate. Plant C is also fed mainly with animal excrement and the second main component is grass silage. Plant D is mainly fed with animal excrement (liquid and solid manure) and maize silage. Plants B to D are representatives of typical German biogas plants as described (see Section 1) because around 70% of the biogas plants are fed with up to 50% excrements (Daniel-Gromke et al 2020). Plant A is an exception as it does not use animal excrement and only a small amount of energy crops. In addition to the feedstocks, data were also collected on the average gas production in the biogas plants. Taking into account the density of the biogas produced, the average amount of digestate formed was calculated using the difference between the feedstock and biogas produced. The monthly digestate formation varied between 5709 tm^{-3} (plant A) and 240 tm^{-3} (plant C). Biogas plants A, B, and D separated the materials from the ST into a solid and a liquid fraction. The investigated material was the solid fraction.

Dry Mass Content

Figure 1 shows the dry mass content of the samples studied. The dry mass content is in the same range for the three separated ST-digestates (ST-S) for plants A, B, and D. As in the material from plant C (ST-L), the liquid fraction is not separated, dry mass content is lower. The digestate from the plants with a separation of liquid and solid fractions has a dry mass content of more than 15%, whereas the material from plant C (without separation) has a dry mass content of 6% only. However, similar dry mass contents were found in all four plants in the process steps F1 and F2, as substrate as well as digestate were treated in the same way in all plants. SD is highest in the samples obtained from plant A. The dry mass content of the solid fraction of the digestate is in the same range as the initial substrates. This is caused by the separation because in general, the fermentation decreases the dry mass content (see Table 1)

Table 2. Relative shares of the input substrates, produced gas, and digestate in the month of sampling at the investigated biogas plants.

—	—	—	Biogas plants			
—	—	—	A	B	C	D
Substrate fresh mass [t/mo.]	—	—	7377	499	290	805
Substrates [%]	Plant silage	Maize silage	23	7	0,06	48
		Grass silage	5	19	43	4
		Whole plant silage	—	29	—	—
		hop vines silage	60	—	—	—
	Solid manure	Horse manure	—	—	19	13
		cattle manure (solid)	—	35	0,1	10
	—	Liquid manure	—	—	36	23
	Other plant material	Sugar beet	—	2	—	—
		Digestate	—	3	—	—
		Corn cob grist	11	—	—	—
		Grain	—	5	2	—
		Grain dust	—	—	—	0,7
Produced gas and digestate	—	Biogas [m^3/mo.]	1,263,322	53,465	37,657	137,962
	—	Digestate fresh mass [t/mo.]	5709	381	240	623

(Zethner et al 2002). The comparison between the separated and unseparated digestate shows that the separation increases the dry mass. For the yield of potential fibers, separation is a helpful process step. If only dry mass content is considered, fiber recovery from the initial substrate would be preferable. Under these circumstances, however, a combination of energy extraction and industrial raw material is not possible.

Cell Wall Components

Figure 2 shows the content of the cell wall components cellulose and lignin, related to the dry

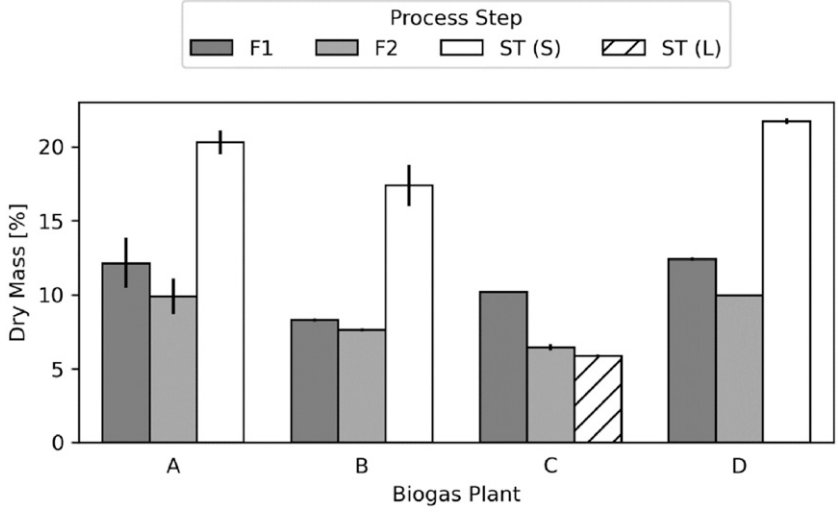

Figure 1. Dry mass content in % of the digestate samples from the investigated biogas plants A-D in the different process steps primary fermenter (F1), secondary fermenter (F2), and storage tank (ST), separated (S) and not separated (L).

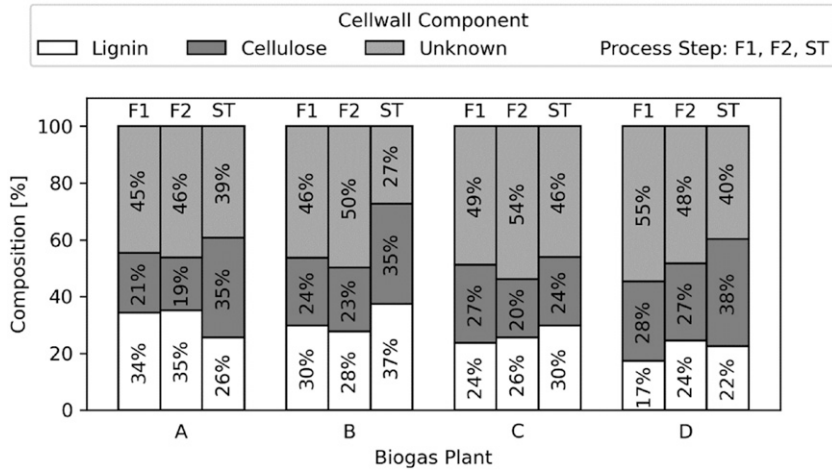

Figure 2. Cell wall composition of the investigated samples of the biogas plants A-D in the process steps primary fermenter (F1), secondary fermenter (F2), and storage tank (ST) related to dry mass.

mass content. To evaluate the fiber quality, shares of cellulose and lignin are most important. In all plants, cell wall content increased during the process, with a higher cell wall content in ST in comparison to F1 samples. The lowest cell wall content was found in D-F1 with 45%.The cellulose content of all samples examined decreases from F1 to F2 and increases again in ST. However, the trend was less clear for the lignin content. In the material from ST, highest lignin content was found in plant B with 37%. Compared with the values of the initial substrates (literature data, see Table 1), the lignin content of the 170 digestates is higher at all process stages and for all plants. The cellulose content of the digestates is similar compared with that of the silages, but clearly higher than that of the animal excrement. This fact is also due to the degradation in the biogas plant. The high proportion of cell wall components is related to their impeded degradation in the fermentation. The remaining biomass is degraded, therefore, the proportion of cell wall substance increases. The reason is that cell wall components are hard to degrade by the microorganisms in the fermentation (Schimpf 2014). Since the content of cellulose and lignin is an important characteristic for natural fibers, the use of digestate is preferable to the use of the initial substrates. The proportions of cellulose and lignin are in the range of wood fibers (see Table 1) in all the samples from process step ST. However, compared with wood fibers, their cellulose content is lower and their lignin content is higher. For a possible application of the digestate fibers in composites, it is positive that the digestate fibers have a similar composition to wood fibers, which are already used (Vogt 2006).

Wet Sieve Analysis

Figure 3 shows the amount of material in the sieves after wet sieving. The percentage of digestate over 1 mm (1and 2 mm mesh size) accounts for more than half of the total fermentation residues in the plants A, B, and D. This result was the same for all process steps and for all three plants. The materials from biogas plant C have a more uniform distribution across all sieves. Only for C-F1 the share of particles on the 2-mm sieve is slightly higher. The proportion of 2-mm fibers decreased from F1 to ST. While more than 80% coarse particles were found in ST, F1, and F2 contained 70% and 60%, respectively. In the case of C, approximately 50% of coarse particles were found for F1, whereas for the other two process stages, only approximately 20% were found. For B, the share of coarse particles varied between 76% (F1) and 47% (ST) depending on process

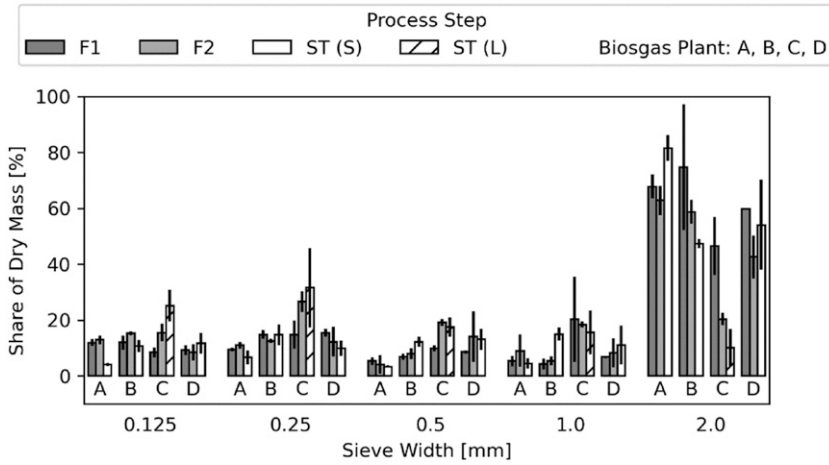

Figure 3. Share of the digestate samples in sieves with different sizes after wet sieving. Biogas plants A-D in the process steps primary fermenter (F1), secondary fermenter (F2), and storage tank (ST), separated (S) and not separated (L) related to dry mass.

step. D did not show such a clear decrease, as more fibers were found in ST with 55% than in F2 with 47%. The lower content of coarse particles in process step ST compared with F1 is caused by the duration of the digestion. The longer the materials remain in the digestion process, the more the plant materials are degraded.

The differences among the biogas plants are caused by the substrates used. Plants B and D were fed with a high proportion of maize silage and plant A shows a high proportion of ensiled hop vines. Both are high-fiber feedstocks, as indicated by literature data in Table 1. Plant C contains a high proportion of 205 manure (liquid and solid) and has fewer coarse particles.

Fiber Geometry

Results of the fiber measurement are presented in Fig 4. Classified by process stage, the fiber length distribution and the degree of slenderness are shown for all studied fermentation residues. Before data analysis, outliers were identified based on the interquartile range and excluded (Frigge et al 1989; Shevlyakov et al 2013). In the figures, only the density function of the length and the slenderness ratio are shown for readability. For fiber length, the functions of the samples from F2 and ST show clear peaks and a small distribution. The material from F1 has a wider fiber length distribution. For the F1 samples from all plants, no clear differences in length distribution were found. The mean fiber length of all samples is approximately 3 mm, and the upper limit is 8-9 mm. In the F2 samples, larger differences in length distribution were found, with a mean fiber length of 4 mm for plant A and a mean fiber length of 2-3 mm for the other plants. The same applies to the upper limit. For plant C it is 6 mm and for plant A 12 mm. The ST-digestates have a similar distribution, except for A-ST. The mean value of C-ST is the lowest with 1.6 mm, whereas the others are in the range of 2-3 mm. In addition to the mean value, the upper limit is also striking. The lowest maximum fiber length was found for C-ST with 4.2 mm, the highest is found for A-ST with 9.5 mm. The mean and maximum values of the slenderness ratio of all samples increased from F1 to F2, but decreased in the last process step ST. D-F1 had the lowest mean slenderness ratio, which is 5, whereas the highest value of 10 was found for B-F1. The fibers of A-F1 showed a wider distribution of the slenderness ratio compared with the other samples. Unlike the others, the function has no peak at one slenderness ratio. The samples from process step ST showed a

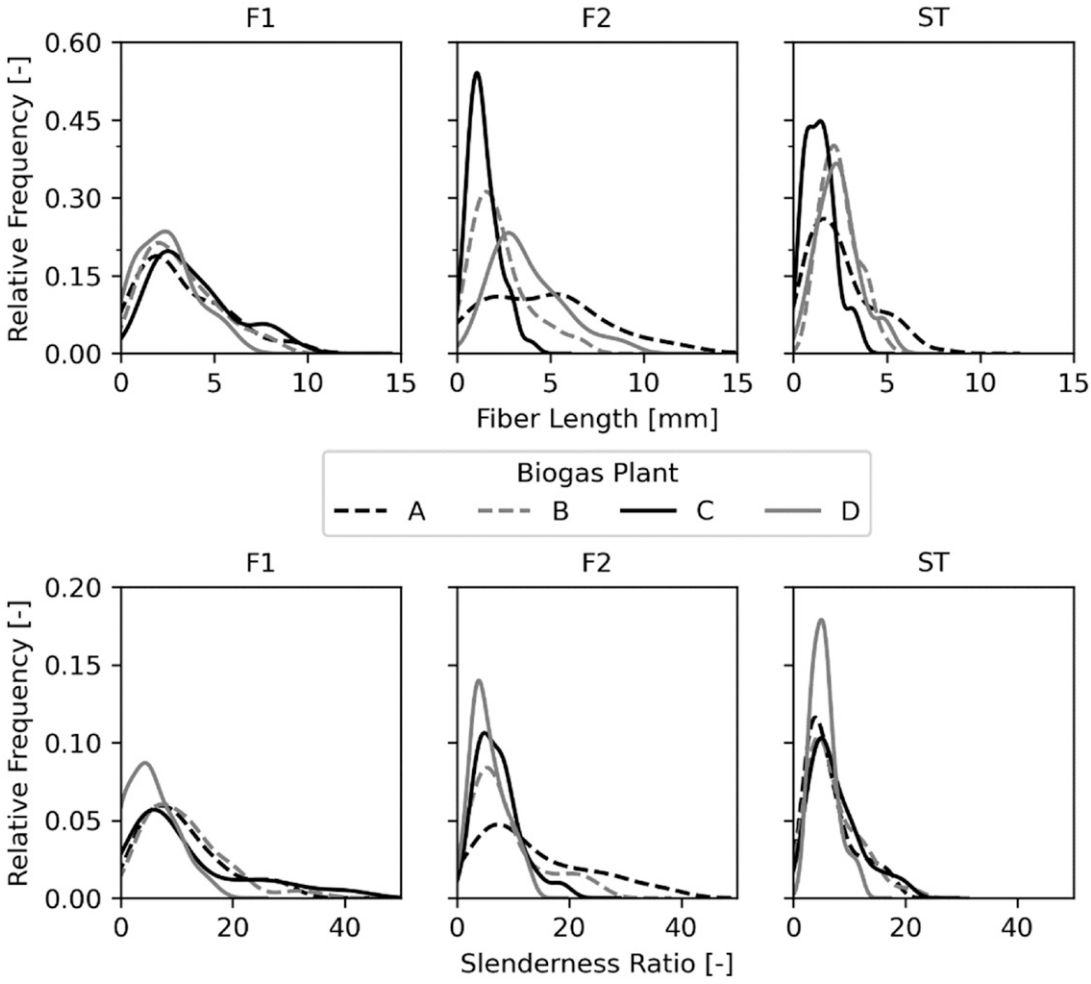

Figure 4. Slenderness–Slenderness and Length deviation of the samples from the four biogas plants in the process steps primary fermenter (F1), secondary fermenter (F2), and storage tank (ST). The three upper diagrams show the length deviation, and the lower diagrams show the slenderness–slenderness deviation.

more equal distribution compared with the previous process steps. The median of all the plants is 5-6, but the maximum values show larger differences. The highest slenderness ratio of the samples D-ST is 13 and not approximately 20 as compared with the other plants. D and C are the plants with the highest proportions of liquid 235 manure, which could potentially explain the difference in the slenderness ratio. The fact that D is the only plant using cereal dust is also an indication of this. In addition, a higher proportion of maize silage is used compared with the other plants. This is also likely a reason for the different geometry of the fibers.

A is the only plant that contains ensiled hop vines, and in a comparatively very high proportion. The presence of the vines also explains the fact that the length and the slenderness ratio in the F2 differ from those of the other plants. The hop vines are the only lignified biomass among the substrates. Due to the different composition, the degradation also differs from that of the less lignified substrates. As with the slenderness ratio, the

Table 3. Density of the dried digestates from the four biogas plants A-D and the three process steps primary fermenter (F1), secondary fermenter (F2), and storage tank (ST).

Biogas plant	A			B			C			D		
Process step	F1	F2	ST	F1	F2	ST	F1	F2	ST	F1	F2	ST
Density (g/cm^3)	1.51	1.53	1.53	1.55	1.54	1.47	1.54	1.54	1.57	1.54	1.54	1.51

different substrate composition may cause different degradation and, thus, also affect the length distribution during the biogas process. However, compared with the common natural fibers, the fibers (see Table 1) are rather short and the length is more similar to the fibers of softwood. For all four plants, most of the fibers have a mean slenderness ratio of at least 5. According to the common definitions for fibers, a large part of the fermentation residue particles, therefore, counts as fibers. On the other hand, they cannot be called textile fibers suitable for textile production, as their slenderness ratio is well below 1000:1. Thicker and short fibers can be used for the nonwoven production (Russell 2006; Fuchs and Albrecht 2012). The fermentation residues meet all the requirements of a fiber and a suitable fiber for nonwoven production. Nonwovens are a common reinforcement for composites (Schürmann 2007). Short fibers and particles like sawmill by-products are commonly used for composites (Vogt 2006). For these reasons, the use of digestate should also be possible.

Density

The density of natural fibers is usually given as 1.5 gcm^{-3}. Table 3 shows the density values of all studied digestate samples. All fermentation residues studied are close to 1.5 gcm^{-3} and are, thus, comparable to other natural fibers. The density is also in the same range independent of plant and process stage. The variations observed are caused by the substrate composition; no trend was observed with respect to the process stage.

Output of Usable Fibers from the Digestate

Using the information obtained from the digestate, listed in Table 1 and the fractions of the sieves with 1- and 2-mm mesh size, the number of usable fibers is estimated. The data of process step ST is used for the calculations because this material is eligible for production. The biogas plants are fed with plant-based biomass and excrements, so the influence of these substrate classes on the fiber output is of interest. Figure 5

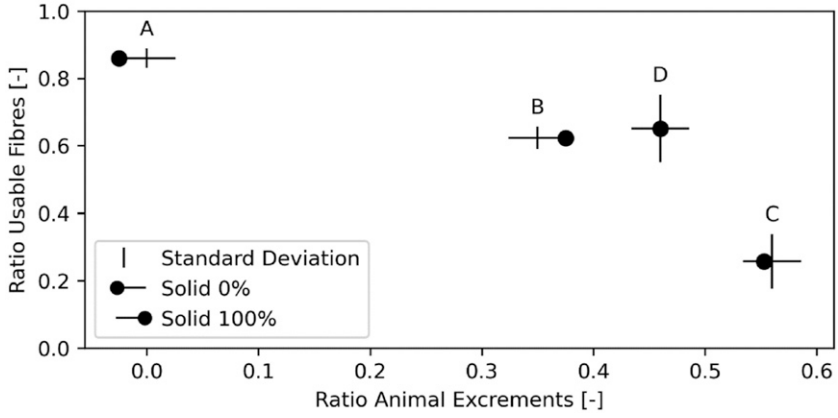

Figure 5. Relationships between quantity of excrements in the substrate and the potential fiber output in the dry mass for the storage tank (ST) samples of the four biogas plants A-D.

shows the relationship between the amount of animal excrement and the ratio of potentially usable fibers in the dry mass of the digestate. With 86%, plant A, the plant without animal excrements, has the highest ratio of potentially usable fibers in the dry mass. The lowest ratio of usable fibers (25%) was found for plant C. The difference between plant B and D is small (62% and 65%). A higher ratio of excrements leads to a higher deviation of the fiber output, compared with plant-based substrates. The more excrement, especially liquid excrement, is included in the substrate mix, the lower is the ratio of usable fibers. Since animal excrement is one of the main initial substrates in German biogas plants (Daniel-Gromke et al 2017), the number of plants with a high output of fibers seems to be low.

CONCLUSIONS

The digestate, according to the general definition, is a fiber with properties similar to those of wood fibers. The initial biogas substrate does not affect the fiber quality, but the quantity of potential fibers. A high proportion of (liquid) animal excrement reduces the quantity of fibers, however, excrement is commonly used. A long time in the biogas plant results in shorter fibers, but the quality (cell wall content) increases. The degradation during the anaerobic digestion cannot fully replace fiber extraction. Because of the high output and the similarity to wood fibers, digestate is an option for composites.

ACKNOWLEDGMENT

This work was funded by the federal ministry for economic affairs and climate action for funding this project (ZIM number 4060062CM9).

The authors thank the following persons or institutions for their help: Mrs. Nadiia Nikulina (Briefing on the test methods) and the Core Facility University Hohenheim (van soest analysis).

REFERENCES

Ahmed Z, Akhter F (2001) Jute retting: An overview. Online J Biol Sci 7:685-688.

AVK (2013) Handbuch Faserverbundkunststoffe/Composites. Springer Vieweg.

BMBF (2020) National Bioeconomy Strategy. https://www.bmbf.de/SharedDocs/Publikationen/de/bmbf/FS/31617_Nationale_Biooekonomiestrategie_Langfassung_en.pdf?__blob=publicationFile&v=5 (26 June 2022).

Bradley WL, Conroy S (2019) Using agricultural waste to create more environmentally friendly and affordable products and help poor coconut farmers. E3S Web of Conferences 130, 1-10.0. National Bioeconomy Strategy.

Crowther J, ed. (1995) Oxford advanced learner's dictionary of current English. Oxford University Press, Oxford, England.

Daniel-Gromke J, Rensberg N, Denysenko V, Barchmann T, Oehmichen K, Beil M, Beyrich W, Krautkremer B, Trommler M, Reinholz T, Vollprecht J, Rühr C (2020) Optionen für Biogas-Bestandsanlagen bis 2030 aus ökonomischer und energiewirtschaftlicher Sicht. Umweltbundesamt.

Daniel-Gromke J, Rensberg N, Denysenko V, Stinner W, Schmalfuß T, Scheftelowitz M, Nelles M, Liebetrau J (2017) Current developments in production and utilization of biogas and biomethane in Germany. Chem Ing Tech 90:17-35.

DIN (2004) DIN EN ISO 1183-2 Kunststoffe- Verfahren zur Bestimmung der Dichte von nicht verschäumten Kunststoffen.

DIN (2006) EN ISO 16472:2006 Animal feeding stuffs—Determination of amylase-treated neutral detergent fibre content (aNDF).

DIN (2008) EN ISO 13906:2008 Animal feeding stuffs—Determination of acid 315 detergent fibre (ADF) and acid detergent lignin (ADL) contents.

Essel R, Breitmayer E, Carus M, Pfemeter A, Bauermeister U (2015) Stoffliche Nutzung lignocellulosehaltiger Gärprodukte für Holzwerkstoffe aus Biogasanlagen. Nova-Institut.

FAO (2021) Data—crops and livestock products—fiber plants. https://fenixservices.fao.org/faostat/static/bulkdownloads/Production_Crops_Livestock_E_All_Data.zip (12 January 2021).

Foreest F (2012) Perspectives for biogas in Europe. The Oxford Institute for Energy Studies, Oxford, UK.

Fortea-Verdejo M, Bumbaris E, Burgstaller C, Bismarck A, Lee KY (2017) Plant fibre-reinforced polymers: Where do we stand in terms of tensile properties? Int Mater Rev 62:441-464.

Frigge M, Hoaglin DC, Iglewicz B (1989) Some implementations of the boxplot. Am Stat 43:50-54.

Fuchs H, Albrecht W, eds. (2012) Vliesstoffe. Wiley-VCH.

Garrote G, Dominquez H, Parajo JC (1999) Hydrothermal processing of lignocellulosic materials. Holz als Roh- und Werkstoff 57:191-202.

Gessner W (1955) Naturfasern Chemiefasern. Fachbuchverlag, Leipzig.

Jain S (2019) Global potential of biogas. The World Biogas Association.

König U, Fudel A (2005) Verfahren zur herstellung von naturfasern aus biogasanlagen und deren Verwendung.

Königsberger S, Deorte M, Reuland G (2019) EBA statistical report 2018. 340 European Biogas Association.

Nielsen Lauge Fuglsang (2005) Composite Materials: Properties as Influenced by Phase Geometry, Berlin: Springer-Verlag, 259 p, ISBN: 9783540243.

Obeng GY, Amoah DY, Opoku R, Sekyere CKK, Adjei EA, Mensah E (2020) Coconut wastes as bioresource for sustainable energy: Quantifying wastes, calorific values and emissions in Ghana. Energies 13(9):2178.

Pfeiffer D, Thrän D, eds. (2015) Messmethodensammlung Biogas. DBFZ.

Riedel U, Nickel J (2000) Konstruktionswerkstoffe aus nachwachsenden Rohstoffen (BioVerbunde). Pages 493-498 in Tagungshandbuch—3. Internationale AVK-TV Tagung für Verstärkte Kunststoffe und Duroplastische Formmassen. doi:10.1002/1521-4052(200105)32:5<493::aid-mawe493>3.0.350co;2-c.

Rueden CT, Schindelin J, Hiner MC, DeZonia BE, Walter AE, Arena ET, Eliceiri KW (2017) ImageJ2: ImageJ for the next generation of scientific image data. BMC Bioinform 18(1):529.

Russell SJ (2006) Handbook of nonwovens. Woodhead.

Salit MS, Jawaid M, Yusoff NB, Hoque ME, eds. (2015) Manufacturing of natural fibre reinforced polymer composites. Springer International Publishing, Cham, Switzerland.

Saville B (1999) Physical testing of textiles. Woodhead, Cambridge, UK.

Scarlat N, Dallemand JF, Fahl F (2018) Biogas: Developments and perspectives in Europe. Renew Energy 129: 457-472.

Schenek A (2001) Naturfaser-Lexikon. Deutscher Fachverlag.

Schimpf U (2014) Enzymatischer Abbau des Lignocellulosekomplexes in Energiepflanzen unter besonderer Berücksichtigung der Silierung und der Biogasproduktion. PhD thesis, Humboldt-Universität zu Berlin.

Schmidt P, Körber R, Coppers M (2003) Sieben und Siebmaschinen. Wiley VCH.

Schuldt A, Dinse R (2010) Ubungen zur Tierernährung im Rahmen deš 370 Moduls Tierernährung und Futtermittelkunde.

Schürmann H (2007) Konstruieren mit Faser-Kunststoff-Verbunden. Springer.

Sergion M, Terrones LAH, Lopes FP, d'Almeida JRM (2005) Mechanical strength of polyester matrix composites reinforced with coconut fiber wastes. Revista Matéria 10:571-576.

Shevlyakov G, Andrea K, Choudur L, Smirnov P, Ulanov A, Vassilieva N (2013) Robust versions of the Tukey boxplot with their application to detection of outliers. Pages 6506-6510 *in* International Conference on Acoustics, Speech and Signal Processing, IEEE. doi:10.1109/icassp.2013.6638919.

Sörgel C, Mantau U, Weimar H (2006) Standorte der Holzwirtschaft—380 Aufkommen von Sägenebenprodukten und Hobelspänen.

Tiefenthaller F (2006) Futterwerttabelle für Wiederkäuer. Landwirtschaftskammer Oberösterreich Abteilung Tierproduktion/Referat Fütterung.

Torrijos M (2016) State of development of biogas production in Europe. Procedia Environ Sci 35:881-889.

Van Soest PJ, Robertson JB (1970) Systems of analysis for evaluating fibrous feeds. Pages 49-60 *in* WJ Pigden, CC Balch and M Graham, eds. Standardization of analytical methodology for feeds. Cornell University, Ithaca, NY.

Ververis C, Georghiou K, Christodoulakis N, Santas P, Santas R (2003) Fiber dimensions, lignin and cellulose content of various plant materials and their suitability for paper production. Ind Crop Prod 19:245-254.

Vogt D (2006) Studie wood plastic composites, Holz-Kunststoff-Verbundwerkstoffe. Landwirtschaftsverlag.

Zethner G, Pfundtner E, Humer J (2002) Qualität von Abfällen aus Biogasanlagen. Umweltbundesamt.

FLEXURAL AND TENSILE PROPERTIES OF 2 × 6 AND 2 × 10 SOUTHERN PINE LUMBER

Marly G. C. Uzcategui
Graduate Research Assistant
E-mail: marlyc17@gmail.com

*Frederico J. N. França**†*
Assistant Professor
E-mail: fn90@msstate.edu

R. Daniel Seale
Warren S. Thompson Professor of Wood Science and Technology
Department of Sustainable Bioproducts
Mississippi State University
Mississippi State, MS 39762-9820
E-mail: rds9@msstate.edu

Christopher Adam Senalik
Supervisory Research General Engineer
E-mail: christopher.a.senalik@usda.gov

Robert J. Ross
Research General Engineer
USDA Forest Products Laboratory
Madison, WI 53726-2398
E-mail: robert.j.ross@usda.gov

(Received August 2022)

Abstract. Bending modulus of elasticity (MOE) and tensile properties parallel to the grain were studied on 702 pieces of 2 × 6 and 285 pieces of 2 × 10 No. 2 visually graded southern pine lumber. The overall rings per inch (RPI) in 2 × 6 pieces was 4.82, whereas 2 × 10 had an RPI average of 3.82. For latewood percentage (LW), 2 × 6 pieces found 45.88% of LW and 45.02% for 2 × 10 pieces. Bending MOE (E_b) mean for 2 × 6 was 10,615 MPa, whereas for 2 × 10 lumber, the mean was 13,665 MPa. The tension MOE (E_t) mean for 2 × 6 lumber was 11,339 MPa, whereas for 2 × 10 the mean was 9735 MPa. The ultimate tensile stress (UTS) mean for 2 × 6 lumber was 28.42 MPa and the overall mean UTS for 2 × 10 lumber was 24.51 MPa. Linear regression models were useful to explain the relationship between E_b and E_t. Strong coefficients of determination ($r^2 = 0.70$ and $r^2 = 0.74$) were found for both lumber sizes between these two properties. Moderate relationships ($r^2 = 0.43$ up to $r^2 = 0.51$) between E_b and UTS were also found for both lumber sizes. However, weaker relationships were found between E_t and UTS ($r^2 = 0.32$ up to $r^2 = 0.40$). Three distributions were fit to the E_b, E_t, and UTS data and evaluated for goodness of fit. The results suggest that E_b of 2 × 6 lumber might be adequately modeled by a normal distribution, and tensile properties of 2 × 10 lumber might be adequately modeled by a lognormal distribution.

Keywords: Bending modulus of elasticity, tension modulus of elasticity, ultimate tensile stress, structural lumber, lognormal distribution.

INTRODUCTION

Southern yellow pine (*Pinus* spp.) is one of the most abundant commercial timber resources in the United States (França et al 2018a; Southern

* Corresponding author
† SWST member

Forest Products Association 2022). From all the grades of southern pine available in the market, No. 2 visually graded lumber remains the most vastly produced lumber. Mechanical properties of southern pine dimensional lumber can be affected by several characteristics though the most commonly associated with the high variation observed in bending and tensile strengths are knots and grain angle. Since design values for southern pine changed in 2012, it is important to continue monitoring the physical and mechanical properties of this timber resource (Gerhards et al 1972; França et al 2018a).

The mechanical properties of lumber vary regardless of the species and size (Forest Products Laboratory 2021). The continuous evaluation of southern pine lumber properties through destructive and nondestructive methods contributes to guaranteeing its quality and maximizing its utility value (França et al 2021). Studying the relationships between lumber properties is essential to deriving allowable properties for lumber (Yang et al 2017). In addition, property relationships, such as the one between modulus of elasticity (MOE) and modulus of rupture (MOR), are frequently used in machine-graded structural lumber. Developing strength property relationships is important because it helps estimate untested properties.

The quality control process for machine-stress-rated (MSR) lumber and machine-evaluated-lumber (MEL) differ in loading methods. For MSR, pieces are tested daily to obtain at least one strength property and MOE in edgewise orientation. On the other hand, MEL requires daily tension quality control alongside tests in edgewise orientation to assess stiffness and bending strength (Forest Products Laboratory 2021). Research on bending and tensile properties allows the wood industry to optimize the sorting processes of lumber. Linear regression models are extensively used to study property relationships because they help reduce costs associated with large lumber-testing programs (Green and Evans 1988; Entsminger et al 2020).

Bending properties include MOE (E_b) and MOR. The MOE is also known as the stiffness of a material. This property is one of the most important because it is a good indicator of load resistance (Wang et al 1993; Nzokou et al 2006; Amishev and Murphy 2008). Stiffness can be determined through static bending or nondestructive tests (Woeste et al 1987; Liliefna 2009). Several authors have conducted studies to analyze the bending property relationships of southern pine lumber (Yang et al 2015, 2017; França et al 2022). Since MOE is used to predict MOR, it is of significant interest to understand the relationship between MOE and tensile properties (Liliefna 2009).

Studies regarding the relationships between MOE and tensile properties are documented in the literature. The study conducted by Doyle and Markwardt (1967) is one of the earliest and most extensive reports on property relationships of southern pine full-size dimensional lumber. Similarly, Green and Kretschmann (1991) and Senalik et al (2020) studied property relationships for southern pine lumber. More specifically, Senalik et al (2020) studied relationships between dynamic MOE and ultimate tensile stress (UTS). Likewise, As et al (2020) and Liliefna (2009) evaluated flexural and tensile property relationships for other commercial softwood species in North America.

The objectives of this study were to: 1) investigate the relationships between bending MOE (E_b) and the properties of tension MOE (E_t) and UTS of 2 × 6 and 2 × 10 No. 2 visually graded southern pine lumber; 2) Summarize the growth characteristics (number of rings per inch [RPI] and percentage of latewood [LW]) presented in the 2 × 6 and 2 × 10 evaluated lumber; 3) assess the statistical distribution of E_b, E_t, and UTS data; and 4) Compare the flexural and tensile properties of 2 × 6 and 2 × 10 southern pine lumber.

MATERIALS AND METHODS

The nominal size for the lumber used in this study was 2 × 6 and 2 × 10, a standardized size that refers to nominal dimensions in inches, where a 2 × 6 is 1.5 × 5.5 inches and 2 × 10 is 1.5 × 9.25 inches. A total of 702 pieces of 2 × 6 and 285 of 2 × 10, No. 2—kiln-dried southern pine lumber were obtained from the 18 commercial

Table 1. Dimensions of 2 × 10 and 2 × 6 southern pine dimensional lumber.

Size (in.)	Thickness (in.)	Width (in.)	Nominal length	Length (m)	Quantity
2 × 6	1.5	5.5	14 ft.	4.27	168
	—	—	16 ft.	4.90	534
2 × 10	1.5	9.25	14 ft.	4.27	85
	—	—	16 ft.	4.88	200

regions of southern pine in the United States (see map França et al 2018b). To verify the grade, all lumber was degraded by a certified grader from either Southern Pine Inspection Bureau (SPIB) or Timber Products Inspection (TP). Table 1 shows the dimensions of the evaluated lumber. Each specimen was labeled at both ends with an identification number. The sample preparation, testing procedures, and statistical analysis performed are summarized as follows:

1. The lumber was conditioned to an average moisture content (MC) of 12%. Lumber was stacked under a covered breezeway to protect it from sun and rain. MC was measured with a moisture meter reader (Wagner model, MMC 220) in all specimens.
2. The RPI were counted at both ends of each specimen following the procedures from SPIB grading rules (SPIB 2014). The total rings counted were divided by the thickness or the width depending on what direction the rings were counted (radial or tangential direction).
3. The LW percentage was determined using the dot grid method as indicated in Uzcategui et al (2020) in accordance with SPIB grading rules (SPIB 2014).
4. Data on width length and thickness, and weight of each specimen was collected to calculate density. The width and thickness were recorded as an average of two readings taken at both ends. The weight was measured with a digital scale.
5. The E_b was measured for all specimens through proof-load bending tests via four-point static tests in edgewise direction using a span-to-depth ratio of 17:1 (see Fig 1[a] and 1[b]). For 2 × 6 lumber, the ratio span was 3.99 m (13.09 ft.), the rate of the load was 0.80000 in/min and the maximum load was 3336 *N*. For 2 × 10 pieces, the span was also 3.99 m while the rate of the load was 0.300 in/min and the maximum load was 4000 *N*. Procedures followed standards ASTM D198-21 (2021) and ASTM D 4761-19 (2019).
6. The E_t and UTS were measured by conducting destructive tests parallel to the grain using a Tension Proof Loader Model 422 (Metriguard, Pullman, USA). Each specimen was placed horizontally in the tension machine

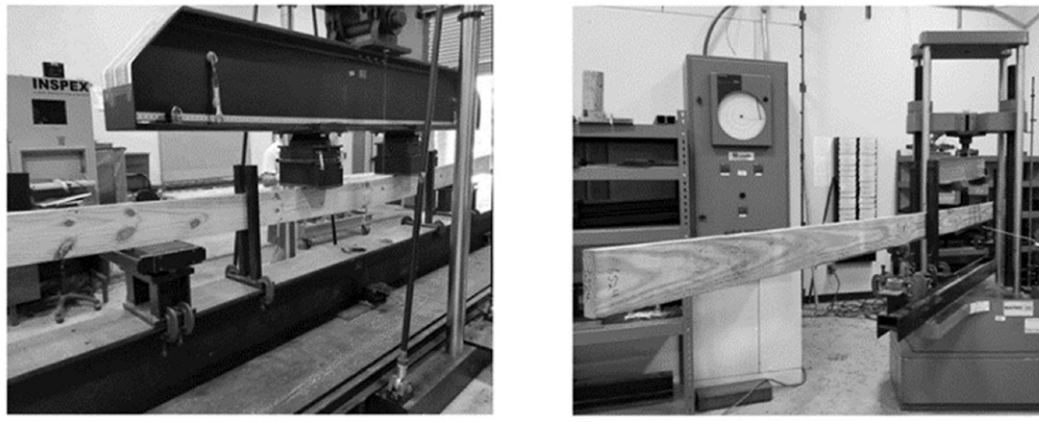

Figure 1. Test setup to determine the flexural modulus of elasticity (MOE or E_b) (Proof-load bending test). (a) Test conducted on 2 × 10 lumber. (b) Test conducted on 2 × 6 lumber.

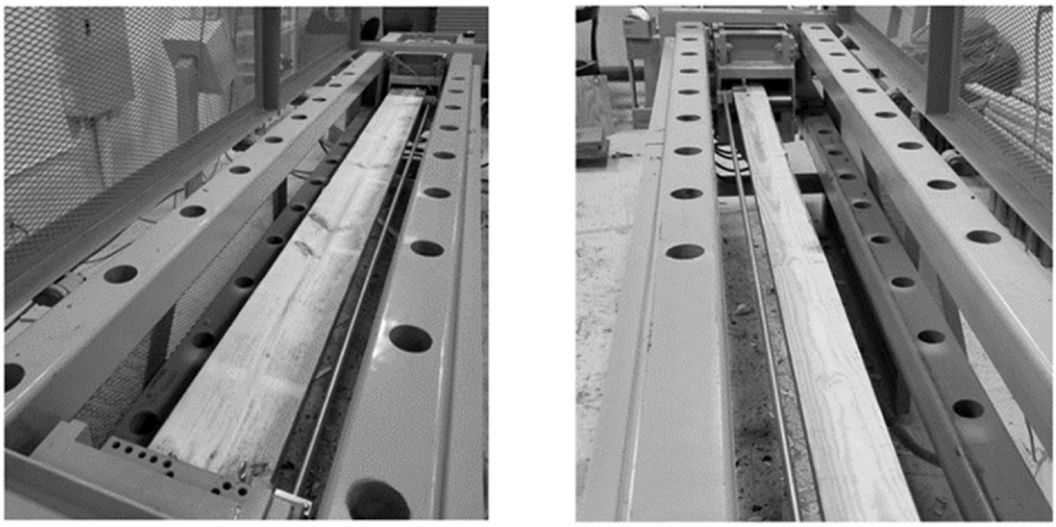

(a) (b)

Figure 2. (a) Test setup used to determine tension parallel to the grain properties of 2 × 10 lumber. (b) 2 × 6 southern pine lumber.

(see Fig 2[a] and 2[b]) and held by metallic grips at both ends while the test was performed. For 2 × 6 and 2 × 10 pieces, the span of testing was 2.44 m (96 in.) for the shorter lumber (14 ft.) and 2.97 m (117 in.) for the longer pieces (16 ft.). Tension tests were performed following the standard D198-21 (ASTM 2021).

7. The statistical software SAS version 9.4 (SAS Institute 2013) was used to obtain descriptive statistics, Analysis of Variance (ANOVA), and linear regression models. ANOVA was calculated at the $\alpha = 0.05$ significance level. The models were created for tensile properties (E_t and UTS) using E_b as the predictor variable. Data was organized taking into consideration the length of each specimen. The coefficient of determination (r^2) was calculated. The E_b, E_t, and UTS data were tested for goodness of fit using the Cramer–von Mises (CVM-sim) test for normal, lognormal, and three-parameter Weibull distributions selected by PROC UNIVARIATE and the histogram option in SAS. Statistical analyses and associated graphs were created following procedures from standard D2915-17 (ASTM 2022).

RESULTS AND DISCUSSION

The physical and mechanical properties of 2 × 6 and 2 × 10 southern pine lumber are summarized in Tables 2 and 3. A preliminary analysis revealed no statistically significant differences between the mechanical properties mean values using the length factor (14 and 16 ft.). For 2 × 6 pieces, the MC mean was 12.20%, the min, was 6.60% and the max was 20.10% with a coefficient of variation (COV) of 17.20%. For 2 × 10 pieces, the MC mean was 11.82% and it ranged between 7.20% and 20.70% with a COV = 18.60%.

Table 2. Overall results for moisture content percent (MC %), density, rings per inch (RPI), and percentage of latewood (LW) on 2 × 6 and 2 × 10 (14 and 16 ft. combined) southern pine dimensional lumber.

	Nominal size	Mean	Min	Max	COV (%)
MC (%)	2 × 6	12.20	6.60	20.10	17.20
	2 × 10	11.82	7.20	20.70	18.60
Density ($kg \cdot m^{-3}$)	2 × 6	560.12	416.00	763.00	9.79
	2 × 10	547.02	436.00	754.00	9.74
RPI	2 × 6	4.82	1.02	18.33	47.40
	2 × 10	3.82	1.67	15.67	48.24
LW (%)	2 × 6	45.88	18.75	82.81	23.62
	2 × 10	45.02	21.09	76.56	21.07

COV, coefficient of variation.

Table 3. Overall results for bending MOE (E_b), tension MOE (E_t), and ultimate tensile stress (UTS) parallel to grain on 2 × 6 and 2 × 10 (14 ft. and 16 ft. combined) southern pine dimensional lumber.

	Nominal size	Mean (MPa)	Min (MPa)	Max (MPa)	COV (%)[a]
Bending	2 × 6	10,615	3994	18,547	24.34
MOE (E_b)	2 ×10	13,365	7162	22,103	21.88
Tension	2 × 6	11,339	3942	22,088	28.30
MOE (E_t)	2 × 10	9735	4415	18,548	25.62
UTS	2 × 6	28.54	5.33	80.14	49.45
	2 × 10	24.42	7.40	72.97	47.67

COV, coefficient of variation.

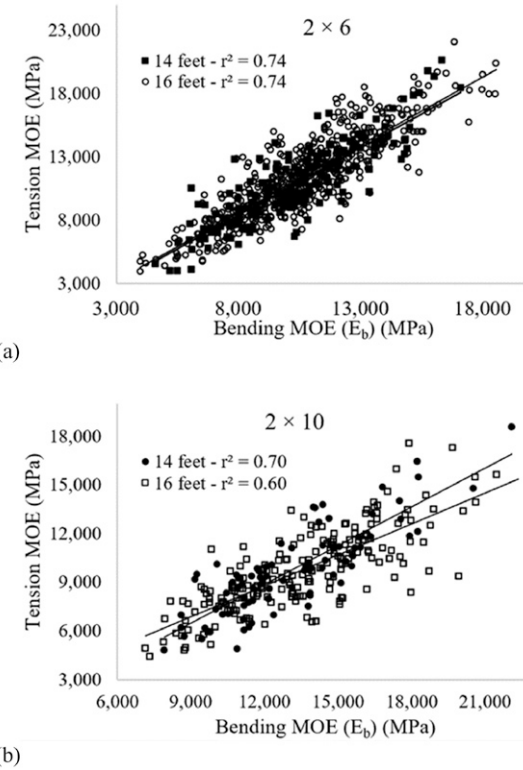

Figure 3. Relationships between bending MOE (E_b) and tension MOE (E_t) for (a) 2 × 6 southern pine pieces; and (b) 2 × 10 southern pine pieces.

For 2 × 6 pieces, the density mean was 560.12 kg·m^{-3}, the min was 416.00 kg·m^{-3} and the max was 763.00 kg·m^{-3} with a COV of 9.79%. For 2 × 10 pieces, the density mean was 547.02 kg·m^{-3}, and it ranged between 436.00 kg·m^{-3} and 754.00 kg·m^{-3} with a COV = 9.74%. The RPI mean, min, and max for 2 × 6 pieces were 4.82, 1.02, and 18.33, respectively. For 2 × 10 pieces, the RPI mean was 3.82 and it ranged between 1.67 and 15.67. The COV obtained from evaluating RPI was over 40% for both lumber sizes.

The LW percentage for 2 × 6 pieces was 45.88%; the min was 18.75%, and the max was 82.81% with a COV of 23.62%. For 2 × 10 pieces, the LW percentage mean, min, and max were 45.02%, 21.09%, and 76.56%, respectively. The COV found for LW percentage on 2 × 10 pieces was 21.07%. Density, RPI, and LW percentage results for both lumber sizes are comparable with the ones reported by Irby et al (2020) and França et al (2018a, 2018b, 2019a, 2019b).

For 2 × 6 pieces, the E_b mean was 10,615 MPa; the min was 3994 MPa and the max was 18,547

Table 4. Values of ANOVA for rings per inch (RPI), percentage of latewood (LW), bending MOE (Eb), tension MOE (Et), and ultimate tensile stress (UTS) depending on the size of lumber.

Property	Factor	DF	SS	MS	F	*p*
RPI	Size	1	205.23	205.23	43.73	<0.0001
	Error	985	4623.09	4.69	—	—
LW (%)	Size	1	148.46	148.46	1.36	0.2446
	Error	985	107,906.35	109.55	—	—
E_b	Size	1	1,540,048,721	1,540,048,721	213.52	<0.0001
	Error	985	7,104,453,605	7,212,643	—	—
E_t	Size	1	521,183,241	521,183,241	57.13	<0.0001
	Error	985	8,986,067,112	9,122,911	—	—
UTS	Size	1	3426.77	3426.77	18.95	<0.0001
	Error	985	178,080	180.79	—	—

DF, degrees of freedom; SS, the sum of squares; MS, mean sum of squares; F, Fisher's F-test; p, significance level.

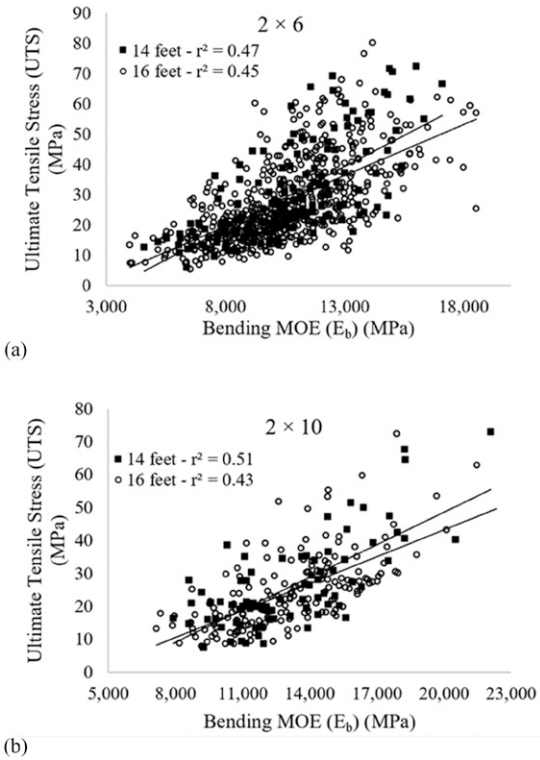

Figure 4. Relationships between bending MOE (E_b) and ultimate tensile stress (UTS) for (a) 2 × 6 southern pine pieces, and (b) 2 × 10 southern pine pieces.

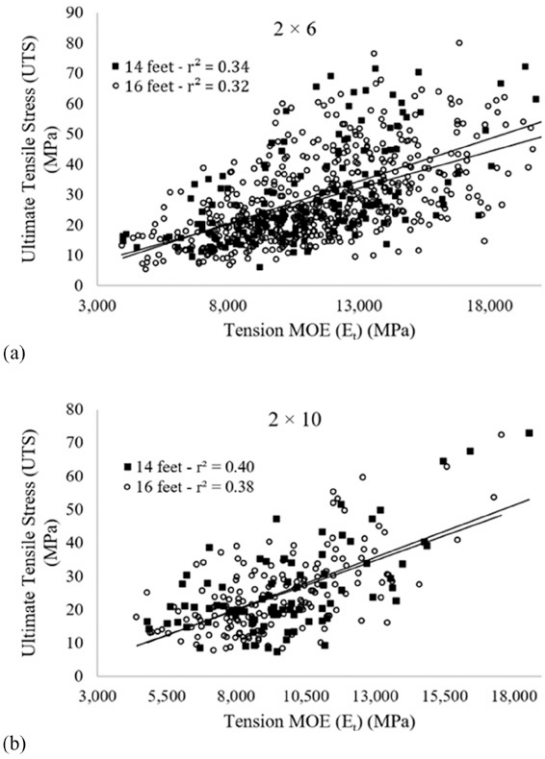

Figure 5. Relationships between tension MOE (E_t) and ultimate tensile stress (UTS) for (a) 2 × 6 southern pine pieces and, (b) 2 × 10 southern pine pieces.

MPa with a COV of 24.34%. For 2 × 10 pieces, the E_b mean, min, and max were 13,365, 7162, and 22,103 MPa, respectively. The COV for 2 × 10 pieces was 21.88%. Overall, the E_b mean value of 2 × 6 pieces is lower than the mean value obtained on 2 × 10 pieces. The E_b results for both lumber sizes are comparable to the ones reported by França et al (2018b, 2019b) and Doyle and Markwardt (1967).

Regarding the tensile properties, the overall mean for E_t on 2 × 6 pieces was 11,339 MPa, ranging from 3942 up to 22,088 MPa with a COV of 28.30%. For 2 × 10 pieces, the mean E_t was 9735 MPa, the min was 4415 MPa and the max was 18,548 MPa with a COV of 25.62%. The UTS mean for 2 × 6 pieces were 28.54 MPa with a min of 5.33 MPa, a max of 80.14 MPa, and a COV of 49.45%. For 2 × 10 pieces, the UTS mean was 24.42 MPa, ranging from 7.40 to 72.97 MPa with a COV of 47.67%. The E_t and UTS mean values obtained on 2 × 6 pieces are slightly higher than the ones for 2 × 10 pieces. Doyle and Markwardt (1967) reported E_t mean values for 2 × 6 and 2 × 8 No. 2 SYP lumber (at 12% MC) that are slightly

Table 5. Summary of the goodness of fit for bending MOE (E_b), tension MOE (E_t), and ultimate tensile stress (UTS) for No. 2 grade southern pine lumber by size.

2 × 6			
Distribution	E_b	E_t	UTS
Normal	0.250[a]	0.038	0.005
Lognormal	0.005	0.005	0.052
Weibull	0.010	0.010	0.010
2 × 10			
Normal	0.028	0.039	0.005
Lognormal	0.037	0.333[a]	0.500[a]
Weibull	0.010	0.010	0.010

[a]Indicates the goodness of fit tests that failed to reject.

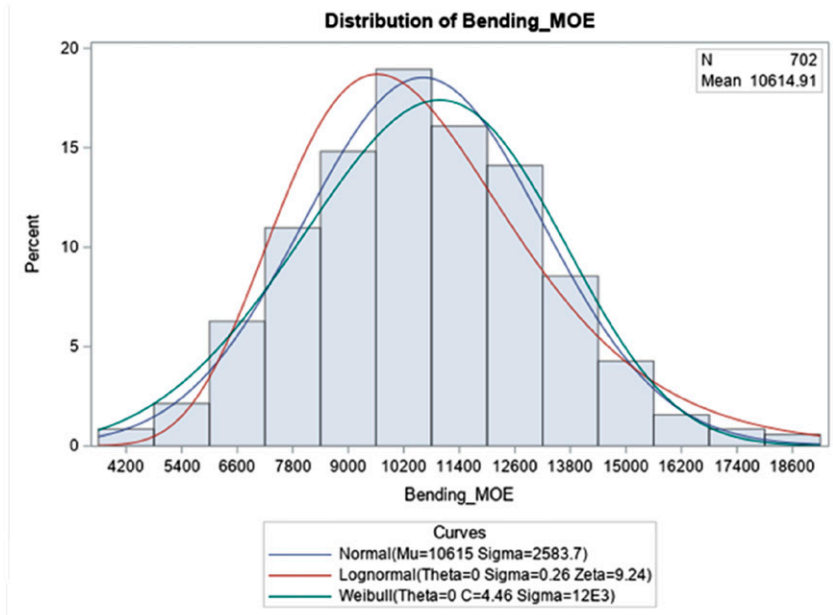

(a)

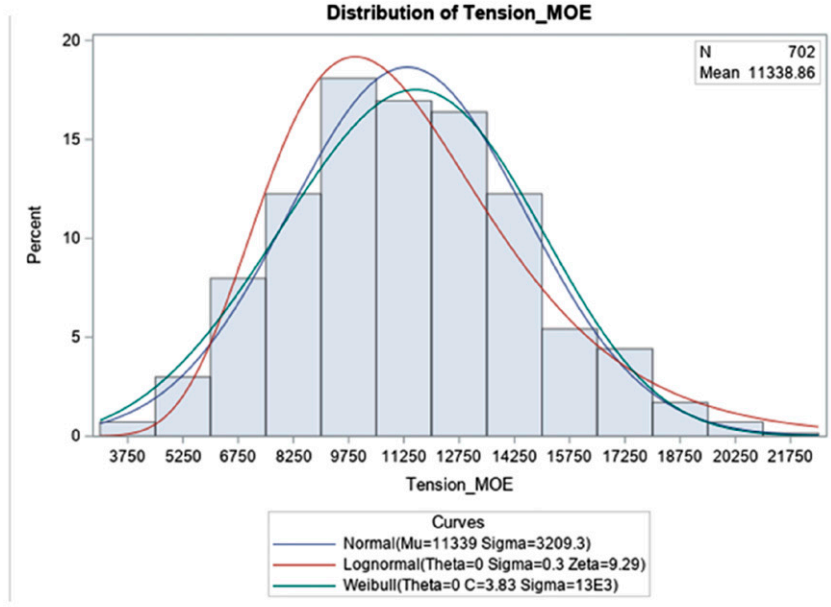

(b)

Figure 6. Distribution of (a) bending MOE (E_b), and (b) tension MOE (E_t), for 2 × 6—No. 2 southern pine lumber.

higher than the ones presented in this study. The same authors reported UTS values that ranged between 6.89 and 71.91 MPa.

An ANOVA was performed to evaluate whether there were significant differences among sizes regarding the growth characteristics and the flexural and tensile properties (see Table 4). The results show that there was a statistically significant difference between RPI ($p = <0.0001$) with respect to the size of the lumber. The RPI for

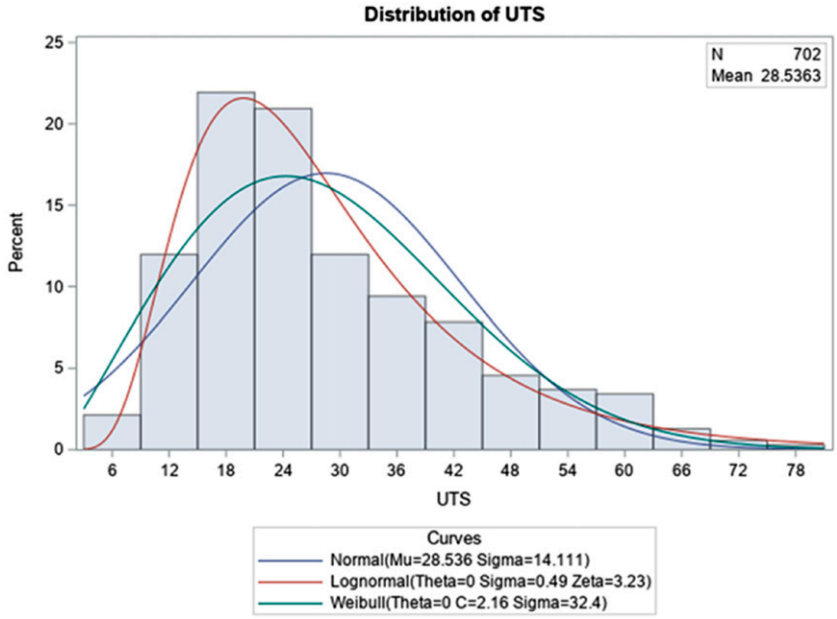

Figure 7. Distribution of ultimate tensile stress (UTS) for 2 × 6—No. 2 southern pine lumber.

2 × 10 lumber (3.82) was significantly lower when compared with the RPI for 2 × 6 lumber (4.82). França et al (2018a) stated that RPI decrease as the width of the pieces increase.

For the LW percentage, no statistically significant difference ($p = 0.2446$) was found between the two sizes. These results agree with França et al (2018a). In relation to the elastic and tensile properties, the results show that there is a statistically significant difference in E_b ($p = <0.0001$), E_t ($p < 0.0001$), and UTS ($p = <0.0001$) with respect to the size of the lumber. The reason for these differences lies in the fact that there is a size-effect regarding the mechanical properties of lumber.

Relationships between Flexural and Tensile Properties

Relationships between E_b and tensile properties are presented in Figs 3-5. Simple linear regression models are used to show the relationship between E_b and E_t, E_b and UTS, and E_t and UTS. Figure 3(a) shows a strong relationship ($r^2 = 0.74$) between E_b and E_t for 2 × 6 lumber (14 and 16 ft.). Figure 3(b) shows a moderate to strong relationship between E_b and E_t for 2 × 10 pieces. The pieces 14 ft. in length showed an $r^2 = 0.70$, whereas the longer pieces had an $r^2 = 0.60$. Doyle and Markwardt (1967) found that E_b and E_t were closely related ($r^2 = 0.88$ for 2 × 6 lumber and $r^2 = 0.94$ for 2 × 8 lumber).

Figure 4(a) and (b) show moderate relationships between E_b and UTS for 2 × 6 and 2 × 10 southern pine pieces (both lengths). For 2 × 6 pieces, the r^2 values were 0.47 and 0.45 for 14 ft. and 16 ft. lumber. For 2 × 10 pieces, the r^2 value for 14 ft. lumber was 0.51, whereas for 16 ft. lumber was 0.43. Doyle and Markwardt (1967) found a weak relationship ($r^2 = 0.30$) between E_b and UTS for 2 × 6 southern pine lumber and a moderate relationship between E_b and UTS ($r^2 = 0.54$) for 2 × 8 lumber. Senalik et al (2020) reported an r^2 value of 0.51 between dynamic MOE and UTS. They also reported an improved r^2 value ($r^2 = 0.71$) including additional parameters from the acoustic properties of lumber.

The relationship between E_t and UTS for 2 × 6 and 2 × 10 southern pine lumber is shown in

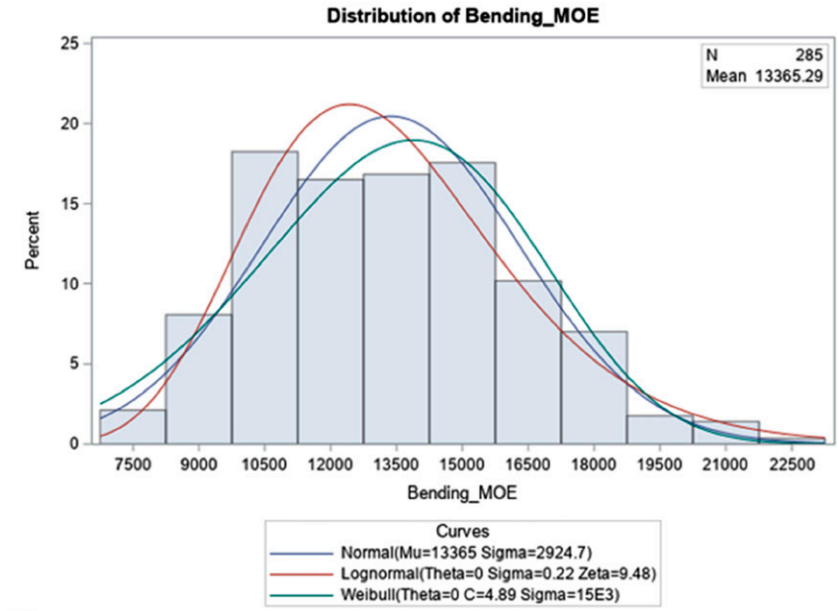

(a)

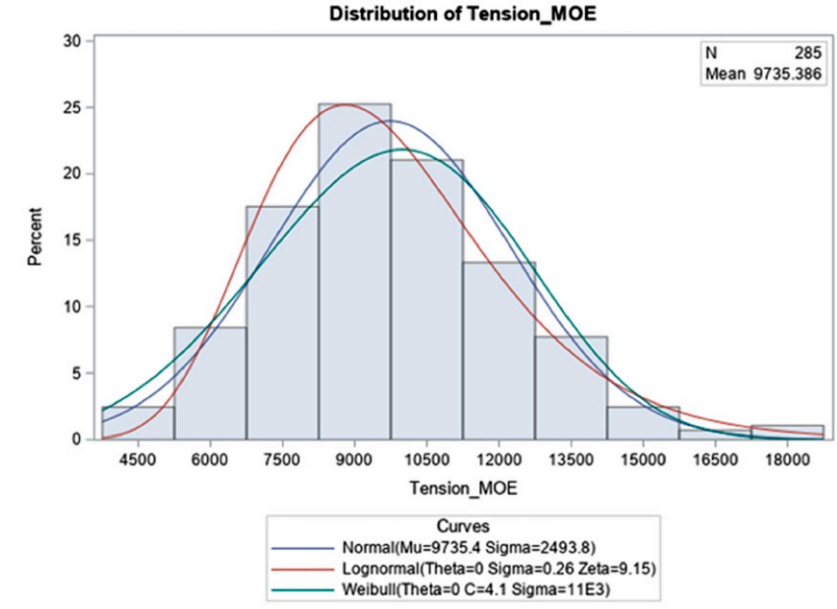

(b)

Figure 8. Distribution of ultimate tensile stress (UTS) for 2 × 6—No. 2 southern pine lumber.

Fig 5(a) and (b). Overall, weak relationships were found between these two properties for either lumber size. For 2 × 6 lumber, r^2 values for 14 and 16 ft. lumber were 0.34 and 0.32 respectively. For 2 × 10 lumber, the r^2 value for 14 ft. lumber was 0.40, whereas for 16 ft. lumber, the r^2 value was 0.38. The r^2 values obtained from the relationship between E_t and UTS for 2 × 10 lumber were slightly higher than the r^2 values obtained for 2 × 6 lumber.

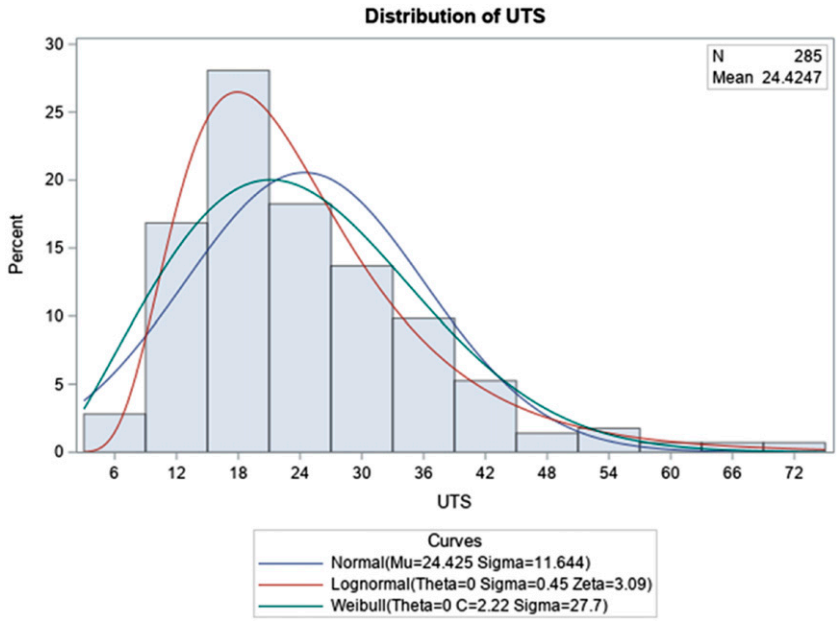

Figure 9. Distribution of ultimate tensile stress (UTS) for 2 × 10—No. 2 southern pine lumber.

Distributions of Flexural and Tensile Properties

Table 5 summarizes the goodness of fit test for E_b E_t and UTS for 2 × 10 and 2 × 6 lumber. For the 2 × 6 lumber, the goodness of fit tests failed to reject the normal distribution for E_b (p = 0.250, Fig 6[a]). The CVM-sim test also showed that Weibull and lognormal distributions are not a good fit for the E_b data for 2 × 6 lumber presented in this study. In contrast, none of the three distributions tested (normal, p = 0.028; lognormal, p = 0.037; Weibull, p = 0.010; Fig 7[a]) adequately fitted the E_b data of 2 × 10 lumber. In contrast, Franca et al (2018a) found that the lognormal distribution fitted the E_b of 2 × 6 lumber while the normal distribution fitted best the E_b of 2 × 10 lumber.

The CVM-sim test indicated that none of the distributions (normal, p = 0.038; lognormal, p = 0.005; Weibull, p = 0.010; Fig 6[b]) appeared to adequately fit the E_t data from 2 × 6 lumber. On the other hand, for the E_t data of 2 × 10 lumber, the goodness of fit tests failed to reject the lognormal (p = 0.33) distribution, whereas the normal (p = 0.039) and Weibull (p = 0.010) distributions were not a good fit (see Fig 7[b]).

For UTS, the CVM-sim tests indicated that none of the three distributions (normal, p = 0.005; lognormal, p = 0.052; Weibull, p = 0.010; Fig 8) adequately fitted the data of the 2 × 6 lumber. However, the lognormal distribution (p = 0.500) was found to be adequate to model the data of 2 × 10 lumber. The normal (p = 0.005) and Weibull (p = 0.010) distributions were not a good fit for the UTS data of 2 × 10 lumber (see Fig 9).

Our results show that no single distribution form fitted all mechanical properties evaluated equally well; however, the lognormal distribution was more predominant. It calls our attention that lognormal distributions only fitted the tensile properties of 2 × 10 lumber. For 2 × 6 lumber, none of the distributions appeared adequately fit the tensile properties; and only the normal distribution was a good match for E_b data. Notably, variation in property distributions can be due to a wide range of factors, which can include mill, time, size, species, and strength-reducing characteristics, such as juvenile wood, the slope of grain,

knots, forest management practices, and so on (McAlister and Clark III 1991; França et al 2018a; Owens et al 2018; Dahlen et al 2012; Verrill et al 2021).

Dahlen et al (2012) reported that the lognormal distribution adequately fitted MOE data of southern pine lumber. Other studies conducted on mill-run lumber populations suggest that mixed normal distributions could be suitable models for elastic properties while skew-normal or mixed normal distributions might be a good match for MOR data (Owens et al 2018, 2019). In Fig 8 and 9, it is clear that the UTS distribution is right-skewed for both lumber sizes. Looking into the distribution shapes for UTS data of 2 × 6 lumber, it is noticeable that the lognormal distribution appears to be the best fit. Recall that the *p*-value for the lognormal distribution was slightly over the 0.05 threshold ($p = 0.052$). Interpretation of this value is at the discretion of the reader.

CONCLUSIONS

This study provides information on the bending MOE and tensile properties of No. 2 visually graded southern pine lumber based on tests conducted on 702 specimens of 2 × 6 and 285 specimens of 2 × 10-dimensional lumber. The material evaluated was obtained from the 18 commercial growing regions of southern pine in the United States. The MC, when tests were performed, was around 12%. Relationships between bending MOE (E_b) and tensile properties (E_t and UTS) parallel to the grain were analyzed. Analysis of the different distribution models for bending and tensile properties was also presented. For both lumber sizes, the following results were obtained:

The RPI mean, min, and max for 2 × 6 pieces were 4.82, 1.02, and 18.33, respectively. For 2 × 10 pieces, the RPI mean was 3.82 and it ranged between 1.67 and 15.67. The COV obtained from evaluating RPI was over 40% for both lumber sizes.

The LW percentage for 2 × 6 pieces was 45.88%; the min was 18.75%, and the max was 82.81% with a COV of 23.62%. For 2 × 10 pieces, the LW percentage mean, min, and max were 45.02%, 21.09%, and 76.56%, respectively. The COV found for LW percentage on 2 × 10 pieces was 21.07%. Density, RPI, and LW percentage results for both lumber sizes are comparable with the ones reported by Irby et al (2020) and França et al (2018a, 2018b, 2019a, 2019b).

1. The overall RPI mean value in 2 × 6 pieces (4.82) was higher than in 2 × 10 pieces (3.82), and the same trend was found for LW, where 2 × 6 pieces (45.88%) had a slightly higher LW percentage when compared with 2 × 10 pieces (45.02%).
2. A close relationship was found between E_b and E_t.
3. Moderate relationships were found between E_b and UTS.
4. Weak relationships were found between E_t and UTS properties.
5. Normal distribution adequately fitted E_b of 2 × 6 lumber.
6. Lognormal distribution adequately fitted E_t and UTS of 2 × 10 lumber.
7. The 2 × 6 pieces had higher Eb values than the 2 × 10 pieces (10,615 and 13,365 MPa, respectively)
8. The 2 × 10 pieces were higher in Et and UTS (11,339 and 28.54 MPa, respectively) when compared with 2 × 6 (9375 and 24 MPa).

ACKNOWLEDGMENT

The authors wish to acknowledge the support of US Department of Agriculture (USDA), Research, Education, and Economics (REE), Agriculture Research Service (ARS), Administrative and Financial Management (AFM), Financial Management and Accounting Division (FMAD), and Grants and Agreements Management Branch (GAMB), under Agreement No. 58-0204-9-164. This paper was approved as journal article SB1066 of the Forest & Wildlife Research Center, Mississippi State University and was received for publication in June 2022. Any opinions, findings, conclusion, or recommendations expressed in this publication are those of the

author(s) and do not necessarily reflect the view of the USDA.

REFERENCES

American Society for Testing and Material (2019) ASTM D4761-19: Mechanical properties of lumber and wood-based structural material. Annual Book of ASTM Standards, West Conshohocken, PA.

American Society for Testing and Material (2021) ASTM D198-21: Standard test methods of static tests of lumber in structural sizes. Annual Book of ASTM Standards, West Conshohocken, PA.

American Society for Testing and Material (2022) ASTM D 2915-17: Standard for sampling and data-analysis for structural wood and wood-based products. Annual Book of ASTM Standards, West Conshohocken, PA.

Amishev D, Murphy GE (2008) In-forest assessment of veneer grade Douglas-fir logs based on acoustic measurement of wood stiffness. Forest Prod J 58(11):42-47.

As N, Senalik CA, Ross RJ, Wang X, Farber B (2020) Nondestructive evaluation of the tensile properties of structural lumber from the spruce-pine-fir species grouping: relationship between modulus of elasticity and ultimate tension stress. Res. Note FPL-RN-0383. Madison, WI: U.S. Department of Agriculture, Forest Service, Forest Products Laboratory. 14 p.

Dahlen J, Jones PD, Seale RD, Shmulsky R (2012) Bending strength and stiffness of in-grade Douglas-fir and southern pine No. 2 2 × 4 lumber. Can J For Res 42(5):858-867.

Doyle DV, Markwardt LJ (1967) Tension parallel-to-grain properties of southern pine dimension lumber. Forest Products Laboratory (U.S.), and U.S Forest Service. Ser. U.S. Forest Service Research Paper FPL, 84, Forest Products Laboratory, Madison, WI.

Entsminger ED, Brashaw BK, Seale RD, Ross RJ (2020) Machine grading of lumber—practical concerns for lumber producers. General Technical Report FPL-GTR-279, U.S. Department of Agriculture, Forest Service, Forest Products Laboratory, Madison, WI. 66 pp.

Forest Products Laboratory (2021) Wood handbook—wood as an engineering material. General Technical Report FPL-GTR-282, U.S. Department of Agriculture, Forest Service, Forest Products Laboratory, Madison, WI. 543 pp.

França FNJ, Seale RD, Ross RJ, Shmulsky R, França TSFA (2018b) Using transverse vibration nondestructive testing techniques to estimate stiffness and strength of southern pine lumber. Forest Service, Forest Products Laboratory, Madison, WI.

França FJN, Seale RD, Shmulsky R, França TSFA (2019a) Modeling mechanical properties of 2 × 4 and 2 × 6 southern pine lumber using longitudinal vibration and visual characteristics. Forest Prod J 68(3):286-294.

França FJN, Seale RD, Shmulsky R, França TSFA (2019b) Assessing southern pine 2 × 4 and 2 × 6 lumber quality: longitudinal and transverse vibration. Wood Fiber Sci 51(1):2-15.

França FJN, Shmulsky R, Ratcliff JT, Farber B, Senalik CA, Ross RJ, Seale RD (2021) Yellow pine small clear flexural properties across five decades. Forest Prod J 71(3):233-239.

França TSFA, França FJN, Seale RD, Ross RJ, Shmulsky R (2022) Flexural properties of visually graded southern pine 2 × 4 and 2 × 6 structural lumber. BioRes 17(1): 1855-1867.

França TSFA, França, FJN, Seale RD, Shmulsky R (2018a) Bending strength and stiffness of No. 2 grade southern pine lumber. Wood Fiber Sci 50(20):1-15.

Gerhards CC, United States Forest Service, Forest Products Laboratory (U.S.) (1972) Relationship of tensile strength of southern pine dimension lumber to inherent characteristics (Ser. U.S.D.A. forest service research paper fpl, 174) Madison, WI: U.S. Department of Agriculture, Forest Service, Forest Products Laboratory.

Green DW, Evans JW (1988) Evaluating lumber properties: Practical concerns and theoretical restraints. Pages 203-217 *in* Proceedings of the 1988 International Conference on Timber Engineering: September 19-22, 1988, Seattle, Washington/Rafik Y. Itani, editor.

Green DW, Kretschmann DE (1991) Lumber property relationships for engineering design standards. Wood and fiber science 23(3):436-456.

Irby NE, França FJN, Barnes HM, Seale RD, Shmulsky R (2020) Effect of growth rings per inch and density on compression parallel to grain in southern pine lumber. BioRes 15(2):2310-2325.

Liliefna LD (2009) Structural property relationships for Canadian dimension lumber. Retrospective Theses and Dissertations, 1919-2007, The University of British Columbia, Vancouver, BC, Canada.

McAlister RH, Clark III A (1991) Effect of geographic location and seed source on the bending properties of juvenile and mature loblolly pine. Forest Prod J 41(9):39-42.

Nzokou P, Freed J, Kamdem DP (2006) Relationship between nondestructive and static modulus of elasticity of commercial wood plastic composites. Holz als roh- und Werkstoff 64(2):90-93.

Owens FC, Verrill SP, Shmulsky R, Kretschmann DE (2018) Distributions of MOE and MOR in a full lumber population. Wood Fiber Sci 50(3):265-279.

Owens FC, Verrill SP, Shmulsky R, Ross RJ (2019) Distributions of modulus of elasticity and modulus of rupture in four mill run lumber populations. Wood Fiber Sci 51(2):183-192.

SAS Institute. (2013). SAS® software, version 9.4. The SAS Institute Inc. Cary, NC.

Senalik CA, França FJN, Seale RD, Ross RJ, Shmulsky R (2020) Estimating lumber properties with acoustic-based technologies-Part 2: Ultimate tension stress estimation from

time- and frequency-domain parameters. Wood Fiber Sci 52(4):390-399.

Southern Forest Products Association (2022) Using southern pine. https://www.southernpine.com/using-southern-pine/ (27 April 2022).

SPIB (2014) Standard grading rules for southern pine lumber. Southern Pine Inspection Bureau, Pensacola, FL.

Uzcategui MGC, Seale RD, França FJN (2020) Physical and mechanical properties of clear wood from red oak and white oak. BioRes 15(3):4960-4971.

Verrill S, Owens FC, Shmulsky R, Ross R (2021) Improved models for predicting the modulus of rupture of lumber under third point loading. Forest Service Research Paper 712:1-38.

Wang Z, Ross RJ, Murphy JF (1993) A comparison of several NDE techniques for determining the modulus of elasticity of lumber. Wood For Res 6(4):86-88.

Woeste FE (1987) Proof loading to assure lumber strength. Madison, WI: Forest Products Laboratory.

Yang BZ, Seale RD, Shmulsky R, Dahlen J, Wang X (2015) Comparison of nondestructive testing methods for evaluating No. 2 southern pine lumber: Part A, modulus of elasticity. Wood Fiber Sci 47(4):375-384.

Yang BZ, Seale RD, Shmulsky R, Dahlen J, Wang X (2017) Comparison of nondestructive testing methods for evaluating No. 2 Southern pine lumber: Part B, modulus of rupture. Wood Fiber Sci 49(2):134-145.

PROFESSIONAL PAGES

SUMMARY OF AWARDS PRESENTED AT 2022 SWST CONVENTION, JULY 10-15, 2022, PEPPERS SALT RESORT AND SPA IN KINGSCLIFF, NSW, AUSTRALIA

GEORGE MARRA EXCELLENCE IN WRITING

The George Marra Award is given in memory of George Marra by the Marra Family in recognition of George's devotion to excellence in writing. Every article in each issue of the most recent volume of Wood and Fiber Science is read and judged by a committee. The committee for 2022 included: Tom Gorman, Prof. Emeritus, University of Idaho, USA and Chair of Committee; Duncan Mayes, Lignutech Oy (Ltd), Finland; Samuel Glass, USDA Forest Products Laboratory, USA; Ilona Peszlen, North Carolina State University, USA.

First Place

Juan L, Bohumil K (2021) Repeatability of adhesion force measurement on wood longitudinal cut cell wall using atomic force microscopy. Wood Fiber Sci 53(1):3-16.

Second Place

Jang E-S, Kang C-W (2021) Effect of porous traits of hardwoods cross-section on sound absorption performance—focusing on six species of Korean hardwoods. Wood Fiber Sci 53(4):260-272.

Third Place

Liu F, Zhang H, Wang X, Jiang F, Yu W, Ross RJ (2021) Acoustic wave propagation in standing trees—Part II. Effects of tree diameter and juvenile wood. Wood Fiber Sci 53(2):95-108.

STUDENT POSTER COMPETITION

The purpose of the Student Poster Competition is to encourage student membership and participation in Society of Wood Science and Technology (SWST), encourage student attendance at the SWST International Conference, recognize excellence in student research, and improve the visibility of student research efforts. A committee of five on a 100-point scale, using the following criteria, evaluated the abstracts and poster presentations:

Submitted Abstract

1. Soundness of research hypothesis (10 points)
2. Scientific writing ability (10 points)
3. Organization (10 points)

Poster Presentation

4. Scientific merit (newness, breadth of interest, and potential impact of the research) (15 points)
5. Experimental design and thoroughness of investigation (15 points)
6. Validity of conclusions (15 points)
7. Organization and visual quality of presentation (15 points)
8. Response to questions of judges (10 points)

This year's panel of student poster judges were: Chair: Eva Haviarova, Purdue University, USA; Lech Muszynski, Oregon State University, USA; Bo Kasal, Fraunhofer-Institut für Holzforschung, Germany; Ilona Peszlen, North Carolina State University, USA; Kyra Wood, University of Tasmania, Australia.

Wood and Fiber Science, 54(4), 2022, pp. 270-274
https://doi.org/10.22382/wfs-2022-25
© 2022 by the Society of Wood Science and Technology

Student Poster Competition Participants

Lilik Astari, University of Melbourne, Australia, *"Suitability of Corn Stalk (Zea mays L.) and Citric Acid Solution for Single Layer Particle Board: Effect of Particle Board Density on Bending Strength and Thickness Swelling"*

Young-Min Cho, Seoul National University, Republic of Korea, *"Study on the Atom Transfer Radical Polymerization According to the Structural Difference of Organosolv Lignin and the Physicochemical Characteristics of Ligno-bioplastics"*

Azin Ettelaei, University of Tasmania, Australia, *"Optimising the Adhesive Performance of Engineered Wood Products Made from Tasmanian Plantation Eucalypt"*

Shofi Fauziyyah, University of Natural Resources and Life Sciences, Vienna, Austria, *"Wood–Water Relationships of Fast-Grown Wood Species Coming from Indonesia and Austria"*

Vikash Ghildiyal, University of Canterbury, New Zealand, *"Strategies for Reducing Drying Collapse in Difficult-to-Dry Plantation Grown Timber"*

Patrick Grant, Queensland University of Technology, Australia, *"Applying Image Analysis Techniques and Spectral Segmentation to Generate a Virtual Board Representation for Simulating Moisture Migration in Laminated Timber Panels"*

Mahboobeh Hemmati, University of Arkansas, United States, *"Life Cycle Assessment of Construction Process in Mass Timber Structure"*

Moein Hemmati, University of Arkansas, United States, *"Comparative Analysis of Thermal Comfort Performance of Wood, Brick, and Concrete"*

Jian Hou, University of Tasmania, Australia, *"Trial Study of the Effect of Glue Type on Finger Joint Strength of E. nitens"*

Jiyao Hu, University of North Texas, United States, *"Binderless Bio-Based Cathode from Wood"*

Trinh Huynh, University of the Sunshine Coast, Australia, *"Multiple Ecosystem Services of Monoculture Hardwood Plantations: A Case Study of Spotted Gum Forests in Queensland"*

Caroline C. Jaozandry, INRAE, France, *"Measurement of Wood Moisture Content: Variations in French Forest Resources"*

Jungkyu Kim, Seoul National University, Republic of Korea, *"Effect of Hemicellulose Hydrolysate Addition on Drying and Redispersion Behavior of Cellulose Nanofibers"*

Yunjin Kim, Seoul National University, Republic of Korea, *"Development Strategy of Cationized Nanocellulose Hydrogel Adsorbent for Effective Cr(VI) Removal"*

Lena Maria Leiter, University of Natural Resources and Life Sciences, Vienna, Austria, *"Dancing Wood Fibers—Engage Children in Wood Science with Triboelectricity"*

Yingwei Liang, University of Tasmania, Australia, *"Serviceability Performance of Cross-Laminated Timber Panels from Fibre-Managed Plantation Hardwood"*

Mengyuan Liu, Tokyo University of Agriculture and Technology, Japan, *"Economic Ripple Effects of Cross-Laminated Timber Manufacturing in Japan"*

Kuluni Millaniyage, University of Tasmania, Australia, *"Comparing the Serviceability of Different Species Used for Flooring Under Extreme Indoor Environmental Conditions: A Tasmanian Case Study"*

Jaewon Oh, Seoul National University, Republic of Korea, *"Greenhouse Gas Emissions and Embodied Energy Analysis of Equivalent Performance Structure Members by Building Material"*

Sangwoo Park, Seoul National University, Republic of Korea, *"Evaluation of Biodegradability and Characterization of Biodegradable Plastic Depending on Lignin Content"*

Lea Primožič, InnoRenew CoE, Slovenia, *"Sustainability Communication of Wood Sector in Comparison to Textile and Car Industry"*

Shaikh Atikur Rahmen, Deakin University, Australia, *"Advanced Finite Element Modelling Technique to Simulate Delamination of Cross-Laminated Timber Under Out of Plane Loading"*

Claudia Roder, University of the Sunshine Coast, Australia, *"Effect of Moisture and Fungal Attack on CLT Connections"*

Nežka Sajinčič, InnoRenew CoE, Slovenia, *"Making Knowledge About Renewable Materials Accessible and Engaging with Educational Videos Based on Instructional Design"*

Morgan Sandera, University of Georgia, United States, *"Comparisons of Wood Quality Among Pines: Naturally Regenerated 1 Longleaf vs Planted Longleaf and Planted Loblolly"*

Jacob Snow, University of Maine, United States, *"Real-Time Monitoring of the Hygrothermal Performance of a CLT School Building"*

Juan Roberto Vargas, University of the Sunshine Coast, Australia, *"Ability of Shallow Preservative Barriers to Protect Eucalyptus Heartwood Timbers: Accelerated Testing"*

Cody Wainscott, Oregon State University, United States, *"In-Depth Characterization of Bondlines in Cross-Laminated Timber Made with Preservative-Treated Lumber"*

Wenxuan Wu, The University of Queensland, Australia, *"Novel Insights Into Self-Sustained Smouldering of CCA-Treated Timber Poles"*

Zidi Yan, University of Queensland, Australia, *"Effect of Repeated Wetting and Drying on Withdrawal Capacity and Corrosion of European Screws in Treated and Untreated Australian Sawn Timber"*

Chae-Hwi Yoon, Seoul National University, Republic of Korea, *"Anti-Inflammatory Effect of Sesquiterpenoids Extracted from Major Coniferous Species in Korea"*

Yuhao Zhang, University of Queensland, Australia, *"Oil Heat Treatment of Timber: Durability Enhancement vs Loss of Mechanical Properties"*

Student Poster Competition Winners

First Place: **Wenxuan Wu**, The University of Queensland, Australia, *"Novel Insights Into Self-Sustained Smouldering of CCA-Treated Timber Poles"*

Second Place: **Cody Wainscott**, Oregon State University, United States, *"In-Depth Characterization of Bondlines in Cross-Laminated Timber Made with Preservative-Treated Lumber"*

Third Place: **Trinh Huynh**, University of the Sunshine Coast, Australia, *"Multiple Ecosystem Services of Monoculture Hardwood Plantations: A Case Study of Spotted Gum Forests in Queensland"*

STUDENT ORAL PRESENTATIONS

In 2021, SWST began awards for student oral presentations to encourage participation and attendance at the SWST International Convention. This year's judges were: Chair: Henry Quesada, Purdue University, USA; Rameez Rameezdeen, University of South Australia, Australia; Tahiana Ramananantoandro, University of Antananarivo, Madagascar; Armando McDonald, University of Idaho, USA; Jan Tippner, Mendel University in Brno, Czech Republic

For 2022, the winners are:

First Place: **Lena Marie Leiter**, University of Natural Resources and Life Sciences, Vienna, Austria, "Developing a Continuous Measurement Setup for Electrostatic Surface Charges, Implemented in Woodworking Processes"
Second Place: **Stavros Spyridakis**, University of Queensland, Australia, "A Novel Bench-Scale Test Method to Characterise the Ignition

Conditions for Timber Protected with Intumescent Coatings"

Third Place: **Juan Roberto Vargas Garcia**, University of the Sunshine Coast, Australia, "Ability of Shallow Preservative Barriers to Protect Australian Eucalyptus Heartwood Timbers: Accelerated Testing"

Distinguished Service Award

The SWST Distinguished Service Award is given in recognition of distinguished service to the profession as a whole and for extraordinary contributions in wood science and technology. Such service may have been made in any educational, technological, scientific, or professional area directly related to the profession of Wood Science and Technology in furtherance of the objectives of the Society as outlined in its Constitution and Bylaws. Guidelines for the award can be found at http://www.swst.org/wp/awards/award-distinguished-service-profession-wood-science-technology/. The 2022 winner is Armando McDonald from the University of Idaho (UI).

Armando McDonald is a professor in Forest and Sustainable Products in the Department of Forest, Rangeland and Fire Sciences at the UI. Armando's comments on his award follow:

I am very honored to be recognized by SWST for this Distinguished service award to the profession of wood science and technology. My career in wood science started at the New Zealand Forest Research Institute (NZ-FRI, now Scion) in 1985 where I was employed as a wood chemist. While at NZ-FRI I honed my skills in wood materials chemistry and wood processing and products by working on various projects. The last few years at NZ-FRI I was project leader of the Biomaterials group. Next, I decided to take the plunge and take up a faculty position in the Department of Forest Products at UI in 2001. Once at UI this exposed me to SWST and its importance in being a member and having an SWST accredited B.S. program in Forest Products. I have been engaged with SWST over the past 2 decades at meetings, judging student presentations, George Marra award committee, and more recently on a multi-university team to increase enrollment of students into wood science/forest products programs both nationally and globally. As part of our SWST accredited program, I teach courses in lignocellulosic biomass chemistry, biocomposites, bioproducts and bioprocessing development (capstone class) and introduction to forest and sustainable products. Teaching is an enjoyable part of being a professor seeing students develop and moving on to their careers in the forest products sector. On the research side of things at UI has been very diverse and invigorating and spans from wood and biomass chemistry, wood composites, bioplastics, wood science, biofuels, lignin-based polymers, fermentation of food waste, waste plastic utilization, municipal solid waste utilization and now to wood based additive manufacturing. This has been (is) achieved by an excellent group of 16 Ph.D. and 20 M.S. students, 6 post-doctoral scholars and 16 visiting scholars over the past 20 years. I think our research efforts will help with developing a biobased circular economy to mitigate climate change.

Fellow Award

The Fellow award recognizes significant contributions to the wood science and technology profession and service to the Society by SWST members. Guidelines and past recipients can be found at http://www.swst.org/wp/awards/swst-fellow-award/. **Fellow Award** was presented to **Eric Hansen** from Oregon State University. Eric has been a strong supporter of SWST since a student, served on numerous SWST committees, was a past President of the Society and serves as the Editor of BioProducts Business.

Distinguished Educator Award

The SWST Distinguished Educator Award is intended to recognize individual faculty and instructors at a university for sustained excellence in teaching or Extension/Outreach programming. Teaching Recognition: The distinguished educator award recognizes sustained excellence in teaching that incites intellectual curiosity in students, inspires colleagues, and makes students aware of significant relationships between the academia and the world. This year's award goes to Gloria Oporto from West Virginia University and Laurence Schimleck from Oregon State University.

Reviewer of the Year Award

In 2019, SWST Executive Board instituted a Reviewer of the Year Award for Wood and Fiber Science. All the issues of 2020 were considered. An honorarium of $300 is awarded to the Reviewer of the Year. This year's award goes to Jilei Zhang from Mississippi State University.

The following criteria is used to judge the Reviewer of the Year Award, which is announced at the annual SWST Meeting:

1. The number of papers reviewed in the previous year.
2. The quality of the review as judged by the editors.
3. Nomination by an author.

All reviewers are ranked according to these criteria and the highest number of points is deemed the Reviewer of the Year.

EDITORIAL AND PUBLICATION POLICY

Wood and Fiber Science as the official publication of the Society of Wood Science and Technology publishes papers with both professional and technical content. Original papers of professional concern, or based on research of international interest dealing with the science, processing, and manufacture of wood and composite products of wood or wood fiber origin will be considered.

All manuscripts are to be written in US English, the text should be proofread by a native speaker of English prior to submission. Any manuscript submitted must be unpublished work not being offered for publication elsewhere.

Papers will be reviewed by referees selected by the editor and will be published in approximately the order in which the final version is received. Research papers will be judged on the basis of their contribution of original data, rigor of analysis, and interpretations of results; in the case of reviews, on their relevancy and completeness.

As of January 1, 2022, Wood and Fiber Science will be an online only, Open Access journal. There will be no print copies. Color photos/graphics will be offered at no additional cost to authors. The Open Access fee will be $1800/article for SWST members and $2000/article for nonmembers. The previous five years of articles are still copyright protected (accept those that are identified as Open Access) and can be accessed through member subscriptions. Once a previous article has reached its 5th anniversary date since publication, it becomes Open Access.

Technical Notes

Authors are invited to submit Technical Notes to the Journal. A Technical Note is a concise description of a new research finding, development, procedure, or device. The length should be **no more than two printed pages** in WFS, which would be five pages or less of double-spaced text (TNR12) with normal margins on 8.5 x 11 paper, including space for figures and tables. In order to meet the limitation on space, figures and tables should be minimized, as should be the introduction, literature review and references. The Journal will attempt to expedite the review and publication process. As with research papers, Technical Notes must be original and go through a similar double-blind, peer review process.

On-line Access to *Wood and Fiber Science* Back Issues

SWST is providing readers with a means of searching all articles in *Wood and Fiber Science* from 1968 to present Articles from 1968 to 2017 are available to anyone, but in order to see 2017 to 2021 articles you must have an SWST membership or subscription. SWST members and subscribers have full search capability and can download PDF versions of the papers If you do not have a membership or subscription, you will not be able to view the full-text pdf.

Visit the SWST website at http://www.swst.org and go to Wood & Fiber Science Online. Click on either SWST Member Publication access (SWST members) or Subscriber Publication access (Institution Access). All must login with their email and password on the HYPERLINK "http://www.swst.org" www.swst.org site, or use their ip authentication if they have a site license.

As an added benefit to our current subscribers, you can now access the electronic version of every printed article along with exciting enhancements that include:

- IP authentication for institutions (only with site license)
- Enhanced search capabilities
- Email alerting of new issues
- Custom links to your favorite titles

(ISSN 0735-6161)
CODEN WOOFAJ

WOOD AND FIBER SCIENCE

JOURNAL OF THE SOCIETY OF WOOD SCIENCE AND TECHNOLOGY

VOLUME 54 OCTOBER 2022 NUMBER 4

CONTENTS